HIGH-SPEED POLARIZATION-SENSITIVE OPTICAL COHERENCE TOMOGRAPHY: TOWARD INTRAOPERATIVE CANCER IMAGING

BY

FREDRICK A. SOUTH

THESIS

Submitted in partial fulfillment of the requirements
for the degree of Master of Science in Electrical and Computer Engineering
in the Graduate College of the
University of Illinois at Urbana-Champaign, 2013

Urbana, Illinois

Adviser:

Professor Stephen Allen Boppart

Abstract

Successful treatment of most breast cancers requires surgical removal of the tumor. The current standard-of-care does not provide any tools for real-time assessment of the tumor cavity. Optical coherence tomography (OCT) has previously been developed for real-time intraoperative use in hopes of aiding tumor margin assessment. While there has been much success, it remains difficult to distinguish between normal stroma tissue and breast cancer.

Polarization-sensitive optical coherence tomography (PS-OCT) is an extension of OCT that measures both the intensity and polarization of light returning from the tissue. PS-OCT is sensitive to changes in collagen structure and may provide additional contrast between normal and diseased tissue. This thesis reports the development of a real-time PS-OCT system using a high-speed swept-source laser and parallel processing on a graphics processing unit (GPU). Results of a preliminary imaging study are also reported, demonstrating that PS-OCT provides enhanced contrast between previously indistinguishable fibrous stroma and invasive ductal carcinoma (IDC).

Acknowledgments

This thesis would not have been possible without the resources, advice, and hands-on help provided by many people. I would like to thank Professor Stephen Boppart for his continual support, resources, and valuable insight. It has been a joy to work in the Biophotonics Imaging Laboratory. I would also like to thank Professor James G. Fujimoto of MIT for providing the FDML laser used in this thesis.

I would like to express my thanks to Professor Steven Adie for our brainstorming sessions, help troubleshooting the FDML laser and system design, and for teaching me to always check my labels. Thanks to Eric Chaney for providing the tissue protocols and for training me in the art of histology. Marina Marjonovic is to be thanked as well for her help in acquiring the tissue imaged in this thesis, and also Darold Spillman for his administrative support. Special thanks to the students, post-docs, and research scientists of the Biophotonics Imaging Lab. Thank you for being supportive and willing to help out at a moment's notice. You make BIL a fun place to work.

I am especially grateful to my family for continual support throughout my life and academic career. Thank you to my father for always looking out for me in the good times and bad. And to my wife for being so supportive and understanding during long hours of homework, imaging, writing, etc. Lastly, thanks to the Lord Jesus Christ who brings meaning to life through service to others. May this work accomplish His goal.

Table of Contents

1 Introduction

1.1 Optical coherence tomography: Application in cancer imaging

Diagnosis and treatment of cancer is one of the greatest challenges facing medicine today. In 2008 an estimated 12.7 million new cancer cases were diagnosed worldwide [1]. Effective treatment of cancer requires early detection followed by biopsy for histological diagnosis of the cancer type. For most solid tumors, it is then necessary to surgically remove the cancerous tissue. During removal of the tumor, it is often difficult to distinguish between healthy and cancerous tissue with the naked eye. Optical imaging has the potential to guide these surgical procedures by providing real-time cellular resolution tomography of biological tissue.

Of the many types of cancer that exist, breast cancer is one of the most common. In 2011 an estimated 300,000 new breast cancer cases were diagnosed in the United States alone, in addition to 40,000 deaths, making breast cancer the second leading cause of cancer deaths among women [2]. X-ray mammography, ultrasound imaging, and magnetic resonance imaging have been very successful at detecting breast cancer early while the tumors are still relatively small. These smaller tumors can be surgically removed while preserving the healthy tissue. A key indicator of local cancer recurrence is the status of the tumor margin [3]. The tumor margin is illustrated in Figure 1.1. A positive or close margin contains cancer cells within a depth of 1 mm from the surface of the resected tissue and leads to repeat surgeries [4, 5]. Unfortunately, positive margins occur in approximately 30% of cases [3].

Ideally, a positive tumor margin would lead to more tissue being resected until the margin is confirmed to be negative. However, the standard of care currently does not include any real-time techniques to evaluate the status of the tumor margin in the operating room. While modalities such as ultrasound imaging and positron emission tomography have been modified for intraoperative imaging, their usefulness is limited by low spatial resolution [6, 7]. Frozen sectioning is somewhat common, but gives poor results when working with adipose tissue which

is common in the breast. Additionally, frozen sectioning increases the surgery time by up to 30 minutes and cannot be considered real-time [8]. Touch prep cytology is an alternative technique that can rapidly assess the margin, but it is only capable of detecting cancer cells on the very surface of the tissue, and requires that the tumor cells slough off [9]. Two-dimensional x-ray projections of the specimen (specimen radiography) also provide quick results but give quite low specificity due to limited resolution, particularly when the margin is not well defined [10, 11].

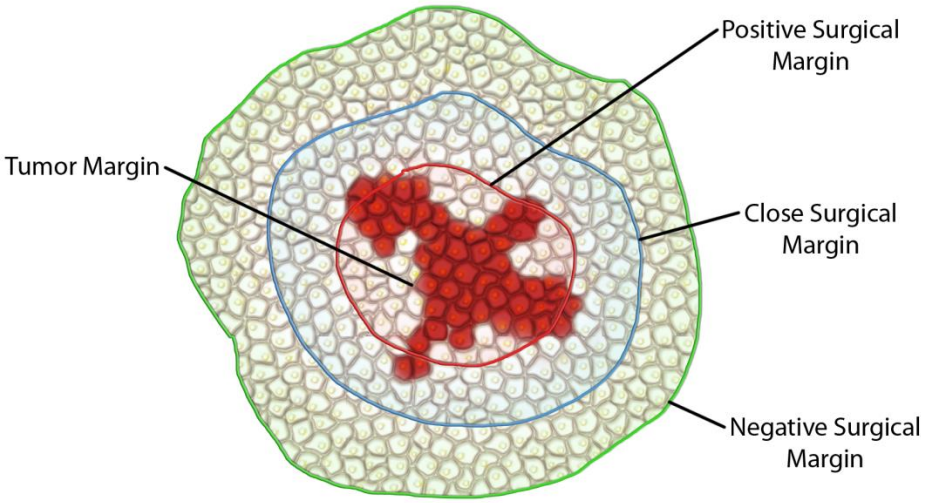

Figure 1.1 Illustration of a resected tissue sample and associated margins. The tumor is indicated by the red cells. A positive surgical margin contains tumor cells at the surface. A close surgical margin contains tumor cells within 1 mm of the surface, while a negative surgical margin does not. Adapted from [12].

Optical coherence tomography (OCT) is a label-free optical imaging modality that detects backscattered near-infrared light to generate three-dimensional images of biological tissue structure [13]. OCT is capable of real-time imaging within 1 mm to 3 mm of the tissue surface, which is ideal for tumor margin assessment [14]. Using pre-clinical cancer models it has been demonstrated that OCT can detect micro-structural changes due to the presence of tumor tissue [15]. Additionally, multiple imaging studies have been conducted on *ex vivo* human breast tissue to explore the differences between normal, pre-cancerous, and cancerous tissue features in OCT [14, 16-18]. It was found that tumor tissue generally appears highly scattering and disrupts the normal adipose and stroma structure. In an intra-operative feasibility study, 37 tumor specimens were imaged immediately following surgical resection [17]. Seventeen of the

specimens were used as a training set. OCT was used to determine the margin status of the remaining 20 specimens. Positive tumor margins were identified with a sensitivity of 100% and a specificity of 82%, suggesting that OCT could be a powerful tool for differentiating tumor and healthy tissue. OCT tumor margin imaging is now being performed *in vivo* to examine the surgical cavity in addition to the resected specimen [19].

Despite these successes, it remains difficult to distinguish between stroma and tumor tissue due to the fact that both appear homogenously scattering when imaged with the several micrometer resolution of OCT. Additionally, normal mammary tissue and cancerous tissue may have similar refractive indices [20]. However, it is possible that differences in collagen structure may provide additional contrast between tissue types. During the growth of a mammary tumor the organization of the surrounding collagen changes significantly. The progression of the tumor associated collagen structure (TACS) may be graded to estimate the severity of the tumor [21]. The advanced TACS stage known as TACS 3 consists of irregularly shaped collagen fibers aligned normal to the tumor boundary. This structure appears to facilitate tumor invasion and can be used as an independent predictor of breast cancer survival [22]. Although this structure is defined on very small scales, similar changes are expected to occur on larger scales as the disease progresses.

Highly anisotropic biological tissues may exhibit form birefringence causing the refractive index to become polarization dependent [23]. Collagen alignment is known to induce form birefringence in tissue. Polarization-sensitive optical coherence tomography (PS-OCT) is a modification of OCT that probes the birefringent properties of biological tissue by measuring the polarization state of the backscattered light [24]. Measurement of collagen content using PS-OCT has previously been demonstrated in atherosclerotic plaques [25]. This suggests that PS-OCT could provide additional contrast for identifying breast cancer. A previously published study found differences between benign fibroadenoma and malignant invasive ductal carcinoma using PS-OCT [26]. However, the relationship to fibrous stroma tissue was not explored, nor was the PS-OCT to collagen relationship histologically confirmed for the various tissue types.

The system developed in this thesis is designed to explore the feasibility of PS-OCT for detecting disease in the breast with a focus on future intraoperative application.

1.2 Optical coherence tomography: Theory and characteristics

Optical coherence tomography is a three-dimensional ranging technique [27]. The foundation for this modality is low-coherence interferometry (LCI). Figure 1.2 is an illustration of the widely used Michelson interferometer. Output from a broadband light source is divided by a beam splitter into two separate paths. The paths will be defined as the sample and reference paths in anticipation of application to OCT imaging. Light in each path is then reflected by a mirror back to the beam splitter where the two beams combine to form an interference signal measured by the photo detector.

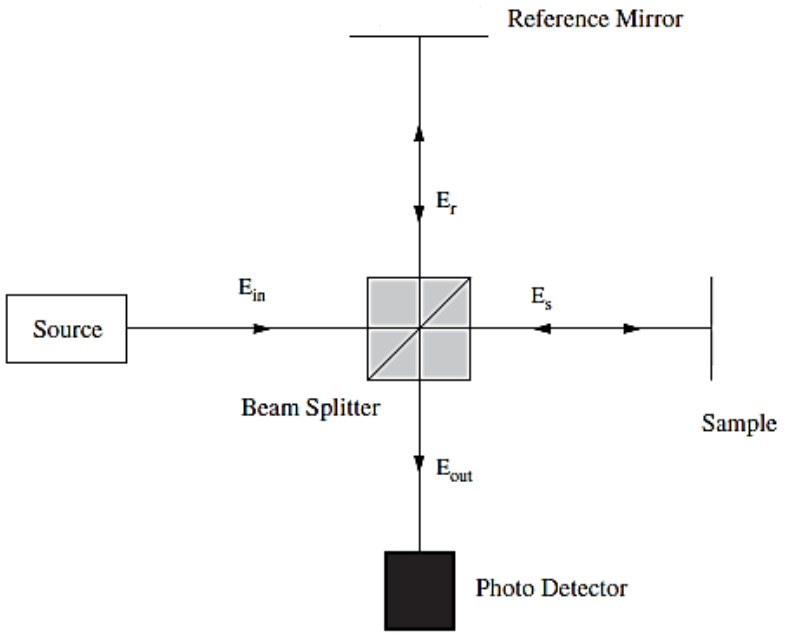

Figure 1.2 Low-coherence interferometer. E_{in}: reference arm field, E_s: sample arm field, E_r: reference arm field, E_{out}: output field. Adapted from [27].

The measured signal is the time averaged intensity of the electric field following combination at the beam splitter. In Equation (1.1), the measured intensity I is given in terms of the reflected reference and sample fields E_R and E_S, where the brackets denote time averaging. The first and second terms denote the intensity of the reference and sample beams. The desired

ranging information is contained in the third term. This is the interference term, which is the real part of the cross-correlation between the two fields.

$$\begin{aligned} I &= \left\langle EE^{*} \right\rangle = \left\langle \left(E_R + E_S\right)\left(E_R + E_S\right)^{*} \right\rangle \\ &= \left\langle E_R {E_R}^{*} \right\rangle + \left\langle E_S {E_S}^{*} \right\rangle + 2\,\mathrm{Re}\left\{ \left\langle E_R {E_S}^{*} \right\rangle \right\} \end{aligned} \tag{1.1}$$

The sample and reference beams will differ only in the distance (optical path length) they have traveled. Therefore, the interference term is equivalent to the real part of Γ, the autocorrelation of the field. The time delay τ between the reference and sample arm is determined by the speed of light c and Δz, the difference in length between the two arms. A factor of two is included to account for the double-pass in each arm. By moving the reference mirror to vary Δz, the coherence function of the source can be measured.

$$\Gamma(\tau) = \left\langle E(t)E(t+\tau) \right\rangle \tag{1.2}$$

$$\tau = 2\left(\frac{\Delta z}{c}\right) \tag{1.3}$$

Optical coherence tomography extends this ranging capability to the imaging of biological tissue. Equation (1.2) defines the response of the ranging system to a perfect reflector. Therefore, the autocorrelation function of the source is the point spread function of the interferometer. The depth structure of the sample tissue at the beam location can be probed by sweeping the reference mirror to change the optical path length in the reference arm. The measured depth structure is then given by the convolution of the true depth structure h with the point spread function Γ.

$$I(\tau) \propto \Gamma(\tau) * h(\tau) \tag{1.4}$$

This method of OCT imaging is known as time domain OCT [13, 27]. This is due to the fact that the depth signal $I(\tau)$ is measured as a function of time while the reference mirror position is used to vary τ. By scanning the beam across the sample in the two transverse dimensions, a three-dimensional map of the tissue reflectance or backscattered intensity can be constructed.

The OCT signal can also be detected in the frequency domain. This can be accomplished by using a diffraction grating to spectrally resolve the interference signal. A CCD line camera can then be used to measure the signal as a function of wavelength. This setup is commonly referred to as spectral domain OCT (SD-OCT) [27]. The frequency domain measurement can also be performed by sweeping the frequency of the source laser and measuring the response in time using a photo detector. This design is referred to as swept-source OCT (SS-OCT) [28]. Both swept-source and spectral domain OCT have a signal-to-noise (SNR) advantage over time domain OCT [29, 30]. Each of the *N* wavelength measurements made can be thought of as an independent interferometry measurement of the sample. As a result, the SNR is improved by a factor of *N*. Because the reference arm remains stationary in SD-OCT, it is possible to achieve very high speeds with excellent stability. The vast majority of recent OCT systems are frequency domain systems for these reasons.

Consider again the Michelson interferometer with a perfect reflector in the sample arm. In the spectral domain, Equation (1.1) becomes a function of frequency ω.

$$I(\omega) = S(\omega) + S(\omega)\left|H(\omega)\right|^2 + 2S(\omega)\left|H(\omega)\right|\cos\left(\phi(\Delta z)\right) \tag{1.5}$$

$$\phi(\Delta z) = 2\left(\frac{\omega \Delta z}{c}\right) \tag{1.6}$$

The terms $S(\omega)$ and $H(\omega)$ refer to the power spectrum of the source and the frequency response of the sample, respectively. The first term in Equation (1.5) is constant throughout the imaging session and is removed via background subtraction, while the second term is typically of negligible intensity. The remaining interference term is a sinusoid whose frequency is dependent upon the difference in path length Δz.

Taking the Fourier transform of the signal transfers the measurement from the frequency domain to the time domain. The time domain signal is a function of τ. Assuming that the spectral response of the sample is relatively uniform over the bandwidths measured, the result is given by Equation (1.7).

$$I(\tau) \propto \Gamma(\tau) * \left[\delta(\tau) + \delta(-\tau)\right] \tag{1.7}$$

The conjugate term is present due to the fact that only the real part of the field is measured. This term is typically zeroed out. Following convolution with the delta function, the result is simply the autocorrelation function as expected. The depth measurement of biological tissue is therefore the same as in Equation (1.4).

Recall that the axial point spread function of the imaging system is the autocorrelation function of the source [31]. The full-width half-max of the autocorrelation function is referred to as the coherence length l_c and is inversely proportional to the source bandwidth $\Delta\lambda$. The resolution is also influenced by the imaging sample's refractive index *n*. For a Gaussian source spectrum with center wavelength λ_0, the coherence length is calculated using Equation (1.8).

$$l_c = \frac{2\ln(2)}{\pi n} \frac{\lambda_0^2}{\Delta\lambda} \tag{1.8}$$

The point spread function in the transverse dimension is decoupled from the axial resolution. Light is focused through an objective lens onto the sample, and the resolution is determined as in a standard microscope. The transverse resolution Δx is given by Abbe's formula.

$$\Delta x = 1.22 \frac{\lambda_0}{2\mathrm{NA}_{obj}} \tag{1.9}$$

The ranging depth of a SD-OCT imaging system is determined by the sample spacing in the frequency domain measurement. Recall Equation (1.5). Each depth in the spatial domain corresponds to a sinusoid in the frequency domain. A higher sampling density will allow the detection of higher frequency components, and therefore greater ranging depths according to the Nyquist sampling theorem. The maximum ranging depth for a system with *N* samples over a bandwidth $\Delta\lambda$ is given by Equation (1.10).

$$z_{\max} = \frac{1}{4} \frac{\lambda_0}{\Delta\lambda} N \tag{1.10}$$

While the ranging depth can be over 10 cm in modern swept-source systems, effective imaging depth is typically much shorter. This is due to the scattering and absorption of the imaging beam. Biological imaging is typically performed in the biological window which includes wavelengths between 800 nm and 1300 nm. This is because several biological components such as blood, melanin pigment, and water are minimally absorbing in this range. A central wavelength near 1300 nm is preferred for bulk tissue imaging because the relative attenuation is lowest in this portion of the biological window [32]. Typical imaging depths are 1-3 mm in highly scattering tissue such as breast tissue, and greater in more transparent structures such as the eye.

1.3 Form birefringence of tissue

The anisotropy of highly organized biological tissue can result in a phenomenon known as form birefringence [23, 33]. Due to the anisotropic boundary conditions, the effective refractive index is polarization dependent, or birefringent. Birefringence in tissue causes the polarization state to change, which is detectable using PS-OCT. Consequently, information about the microstructure of the tissue can be inferred from the PS-OCT measurement.

Muscle is an example of a highly anisotropic and birefringent biological tissue. A pervious study imaged both healthy and diseased mouse muscle using PS-OCT and found significant differences in the PS-OCT image [34]. Figure 1.3 shows both OCT and PS-OCT images of exercised healthy mouse muscle. The organized muscle fibers lead to strong birefringence, evidenced by the banding pattern in the PS-OCT image. A muscular dystrophy mouse model was also exercised then sacrificed for imaging. The resulting PS-OCT image in Figure 1.4 shows significantly decreased birefringence. This study demonstrated that microstructural changes beyond the resolution limit of structural OCT can be inferred using PS-OCT measurement of form birefringence.

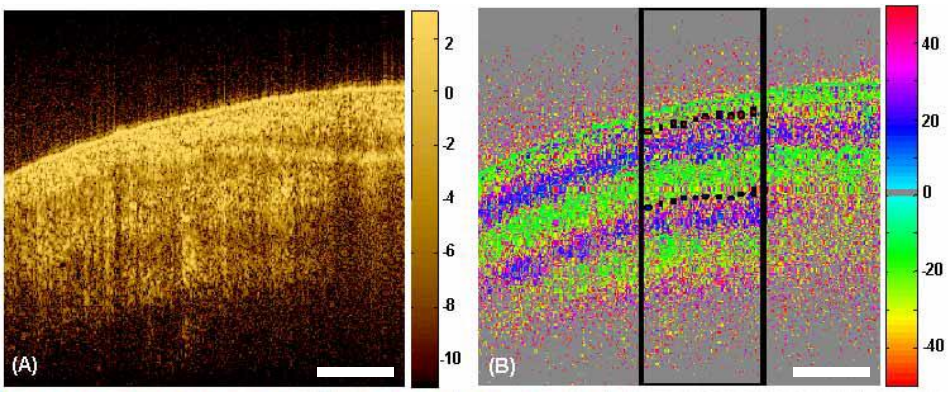

Figure 1.3 Exercised healthy mouse muscle. (A) Structural OCT image. (B) PS-OCT phase retardation image. Scale bars correspond to 500 µm. Adapted from [34].

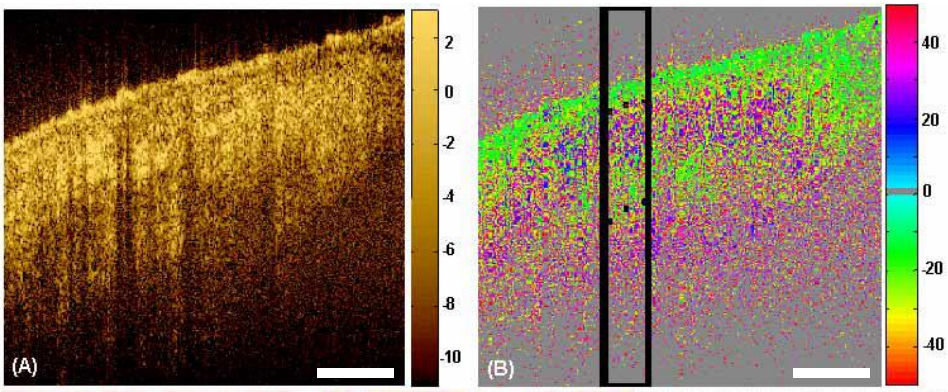

Figure 1.4 Exercised muscle of muscular dystrophy mouse model. (A) Structural OCT image. (B) PS-OCT phase retardation image. Scale bars correspond to 500 µm. Adapted from [34].

Dense, organized collagen fibers are also birefringent and can therefore be used as a source of contrast in PS-OCT imaging. Previously published work has demonstrated PS-OCT contrast in fibrous atherosclerotic plaques [25]. When the collagen content of the plaque decreases, the plaque may become unstable and break away leading to dangerous complications. Figure 1.5 demonstrates the correlation between the PS-OCT signal and collagen content. The highly fibrous plaque contains a dense collagen population, leading to high birefringence in comparison with the less fibrous plaque.

These previous studies demonstrate that the form birefringence of collagen can be measured using PS-OCT. This thesis will explore form birefringence as a method of contrast for breast cancer imaging.

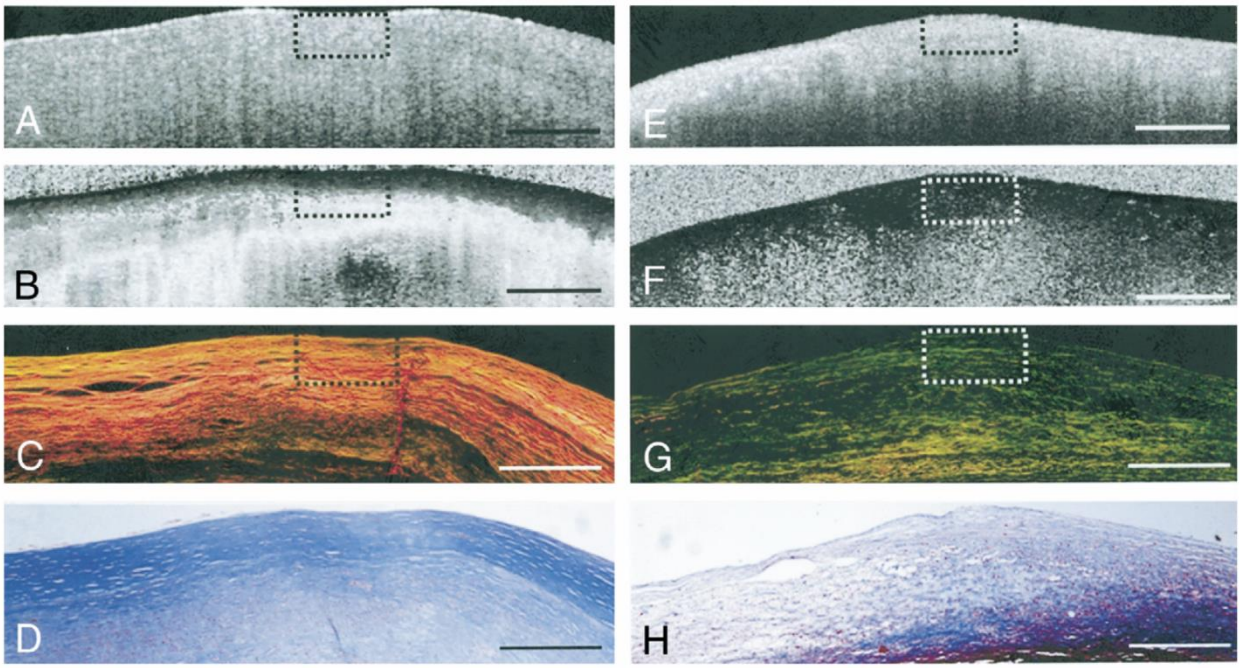

Figure 1.5 Birefringence of fibrous plaques. (A) and (E) structural OCT image. (B) and (F) PS-OCT phase retardation image. (C) and (G) picrosirius red histology stain. (D) and (H) trichrome histology stain. Scale bars correspond to 500 µm [25].

1.4 Statement of work

The purpose of this research is to develop a high-speed PS-OCT imaging system to explore applications in breast cancer imaging with potential for future intraoperative application. This PS-OCT imaging system will provide new structural contrast from tissue birefringence in addition to standard structural imaging based on refractive index variations within the tissue, giving additional information about the tissue microstructure. The high-speed imaging and processing capabilities are developed in anticipation of intraoperative application. This high-speed capability is necessary to help alleviate the effects of motion artifacts and provide real-time display.

Chapter 2 of this thesis will address the mathematical representation of polarization in optical systems. This mathematical foundation will then be used to describe the theory and implementation of PS-OCT in Chapter 3. The specific swept-source implementation developed for this thesis will be addressed in Chapter 4. Chapter 5 will present the results of PS-OCT

imaging in human breast tissue. A summary of the presented work and suggestions for future work will be given in Chapter 6.

2 Polarization Theory of Light

2.1 Polarization of light

In many optical imaging applications, light is treated as a scalar wave. However, it can be seen from Maxwell's equations that light is necessarily a transverse wave, meaning that the electric and magnetic field vectors are orthogonal to the direction of propagation [35]. To more accurately model the interaction between light and biological samples, it is necessary to carefully consider this transverse wave nature of light. In this chapter, the interaction between the light vector and matter will be put into a mathematical framework that will allow simplified discussion of PS-OCT systems in the following chapters.

When light interacts with a material, it induces an electric field displacement **D** as shown in Equation (2.1). The incident electric field is represented by **E** and the vacuum permittivity by ε_0. Of particular interest is the field displacement due to the material properties. This is encoded in the polarization density **P**. The incident electric field creates a multitude of electric dipole moments in the material that combine to create a macroscopic polarization density. In Equation (2.2), it is shown that the polarization density is dependent upon $\overline{\overline{\chi}}$, the electric susceptibility of the material.

$$\mathbf{D} = \varepsilon_0 \mathbf{E} + \mathbf{P} \tag{2.1}$$

$$\mathbf{P} = \varepsilon_0 \overline{\overline{\chi}} \mathbf{E} \tag{2.2}$$

Since the electric field **E** is necessarily a vector, it follows that the susceptibility $\overline{\overline{\chi}}$ must be tensor valued. The tensor can be represented by a Hermitian symmetric matrix. Equation (2.2) can then be expanded as shown in Equation (2.3).

$$\begin{bmatrix} P_x \\ P_y \\ P_z \end{bmatrix} = \varepsilon_0 \begin{bmatrix} \chi_{xx} & \chi_{xy} & \chi_{xy} \\ \chi_{yx} & \chi_{yy} & \chi_{yz} \\ \chi_{zx} & \chi_{zy} & \chi_{zz} \end{bmatrix} \begin{bmatrix} E_x \\ E_y \\ E_z \end{bmatrix} \tag{2.3}$$

The susceptibility tensor can then be diagonalized using eigenvalue decomposition resulting in Equations (2.4) and (2.5) where α, β, and γ are standard Euler angles of rotation.

These equations highlight the fact that the optical behavior of an anisotropic material is dependent upon the orientation, or polarization, of the electric field vector.

$$\overline{\overline{\chi}} = \mathbf{R}(\alpha,\beta,\gamma)\begin{bmatrix} \chi_{xx} & 0 & 0 \\ 0 & \chi_{yy} & 0 \\ 0 & 0 & \chi_{zz} \end{bmatrix}\mathbf{R}^{-1}(\alpha,\beta,\gamma) \tag{2.4}$$

$$\mathbf{R}(\alpha,\beta,\gamma) = \begin{pmatrix} \cos\alpha\cos\gamma - \sin\alpha\cos\beta\sin\gamma & -\sin\alpha\cos\gamma - \cos\alpha\cos\beta\sin\gamma & \sin\beta\sin\gamma \\ \cos\alpha\cos\gamma + \sin\alpha\cos\beta\sin\gamma & -\sin\alpha\cos\gamma + \cos\alpha\cos\beta\sin\gamma & -\sin\beta\sin\gamma \\ \sin\alpha\sin\beta & \cos\alpha\sin\beta & \cos\beta \end{pmatrix} \tag{2.5}$$

When the three eigenvalues of the susceptibility tensor are equal, the material is isotropic and the problem can be treated as in the scalar case. If any of the eigenvalues differ, the material is anisotropic and the electric field polarization must be considered. When $\chi_{xx} \neq \chi_{yy} = \chi_{zz}$, the material is said to be uniaxial. In the case where $\chi_{xx} \neq \chi_{yy} \neq \chi_{zz}$, the material is biaxial.

In optics it is common to discuss material properties in terms of refractive index. The refractive index is directly related to the susceptibility by Equation (2.6).

$$n = \sqrt{(1+\chi)} \tag{2.6}$$

A uniaxial crystal will have two different refractive indices. As an example, consider the case where $n_x < n_y = n_z$. The *x*-axis has the lowest refractive index and is known as the optic axis or fast axis because light propagates with the highest velocity along this direction. The *y*-*z* plane is known as the slow axis.

Note that this derivation has not mentioned the effects of the magnetic field. At optical frequencies the relative magnetic permeability μ_r is approximately equal to one [35]. In this case it is safe to assume that the magnetic field does not interact with the material.

2.2 Jones calculus

Consider an optical setup in a Cartesian coordinate system with an optical wave propagating along the positive *z* direction. The electric field vector is then restricted to the *x*-*y* plane. Equation (2.3) then simplifies to Equation (2.7).

$$\begin{bmatrix} P_x \\ P_y \end{bmatrix} = \varepsilon_0 \begin{bmatrix} \chi_{xx} & \chi_{xy} \\ \chi_{yx} & \chi_{yy} \end{bmatrix} \begin{bmatrix} E_x \\ E_y \end{bmatrix} \tag{2.7}$$

We are therefore limited to measuring birefringence in the *x*-*y* plane. This setup is useful for describing many experimental setups using components such as optical retarders, polarizers, and rotators.

This basic setup is the foundation for a mathematical description of polarization known as Jones calculus. In a series of papers by Jones, this setup was examined to create an algebraic method for calculating the propagation of polarization states through optical components [36-39]. A polarized optical wave can be decomposed into two orthogonal components. For simplicity, we will consider the linearly polarized components in the *x* and *y* directions as our basis elements. However, there are many other valid choices including right-hand and left-hand circularly polarized light. The decomposition shown in Equation (2.8) can be rewritten in the form of a Jones vector, as seen in Equation (2.9).

$$\mathbf{E} = Ae^{i\phi} = A_x e^{i\phi_x}\hat{\mathbf{x}} + A_y e^{i\phi_y}\hat{\mathbf{y}} \tag{2.8}$$

$$\mathbf{E} = \begin{bmatrix} E_x \\ E_y \end{bmatrix} = \begin{bmatrix} A_x e^{i\phi_x} \\ A_y e^{i\phi_y} \end{bmatrix} \tag{2.9}$$

The vector magnitudes and phases in the *x* and *y* directions are given by A_x, ϕ_x, A_y, and ϕ_y. The relative magnitude and phase of the *x* and *y* components define the polarization state of the light. As was stated above, the basis vectors for our Jones vector are horizontal and vertically polarized light. These correspond to $\mathbf{E} = \begin{bmatrix} 1 & 0 \end{bmatrix}^{\mathrm{T}}$ and $\mathbf{E} = \begin{bmatrix} 0 & 1 \end{bmatrix}^{\mathrm{T}}$, respectively.

When both the horizontal and vertical (*x* and *y*) components are non-zero, the polarization state can be further defined by the ratio of magnitudes A_x / A_y and the phase difference $\Delta\phi = \phi_x - \phi_y$. For all linear polarization states, $\Delta\phi$ is an integer multiple of π. The angle θ at which the light is linearly polarized determines the ratio of the magnitudes as shown in Equation (2.10).

$$\mathbf{E} = \begin{bmatrix} \cos\theta \\ \pm\sin\theta \end{bmatrix} \tag{2.10}$$

A special case known as circularly polarized light occurs when A_x is equal to A_y and $\Delta\phi$ is an integer multiple of $\pi/2$. In this case, the electric field vector traces out a circular pattern as it propagates. There are various conventions that can be used to define the handedness of the circular polarization state. We will consider the polarization state from the view of the receiver or observer far along the *z*-axis looking back toward the optical system. In this setup, the light is propagating toward the observer. When the polarization rotates clockwise (*y* leads *x*), it is known as right-hand circularly polarized light. Counterclockwise rotation (*x* leads *y*) is known as left-hand circularly polarized. Using the convention that a phase delay is represented as $e^{-i\phi}$, the resulting circular polarization states are represented by the Jones vectors given in Equations (2.11) and (2.12). The multiplicative factor is included to ensure unit magnitude of the Jones vector. As is typically done in the Jones vector notation, only the relative phases are indicated. The common phase due to propagation is ignored.

$$\mathbf{E}_{right-circular} = \frac{1}{\sqrt{2}}\begin{bmatrix} 1 \\ i \end{bmatrix} \tag{2.11}$$

$$\mathbf{E}_{left-circular} = \frac{1}{\sqrt{2}}\begin{bmatrix} 1 \\ -i \end{bmatrix} \tag{2.12}$$

The most general case is known as elliptically polarized light. In this case, the relationships described above for linear and circularly polarized light no longer hold. The result is that the electric field vector traces out an ellipse as it propagates.

To summarize the discussion above and to provide a more intuitive understanding of the Jones vector, illustrations of many polarization states along with their corresponding Jones vectors are shown in Figure 2.1. The illustration indicates the pattern the electric field vector traces out as it propagates toward the observer. Each illustration corresponds to the Jones vector directly below.

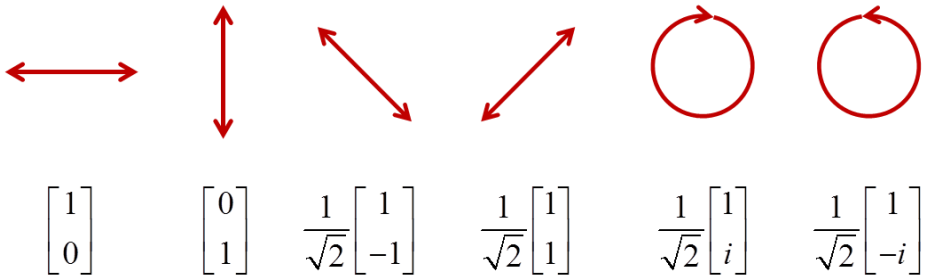

$$\begin{bmatrix}1\\0\end{bmatrix} \quad \begin{bmatrix}0\\1\end{bmatrix} \quad \frac{1}{\sqrt{2}}\begin{bmatrix}1\\-1\end{bmatrix} \quad \frac{1}{\sqrt{2}}\begin{bmatrix}1\\1\end{bmatrix} \quad \frac{1}{\sqrt{2}}\begin{bmatrix}1\\i\end{bmatrix} \quad \frac{1}{\sqrt{2}}\begin{bmatrix}1\\-i\end{bmatrix}$$

Figure 2.1 Illustrations of several common polarization states and their corresponding Jones vector representations.

To represent an optical element that affects the polarization state of light, we desire a linear operator that will act upon the Jones vector. This operator is known as the Jones matrix. The two-by-two Jones matrix **J** acts upon the two-by-one Jones vector **E**, resulting in an output Jones vector $\mathbf{E}'$. This operation is shown in Equations (2.13) and (2.14).

$$\mathbf{E}' = \mathbf{JE} \tag{2.13}$$

$$\begin{bmatrix}E_x'\\E_y'\end{bmatrix} = \begin{bmatrix}J_{11} & J_{12}\\J_{21} & J_{22}\end{bmatrix}\begin{bmatrix}E_x\\E_y\end{bmatrix} \tag{2.14}$$

The simplest Jones matrix is that of a polarizer. A linear polarizer located along the horizontal (*x*-axis) is represented by a Jones matrix with a single nonzero value.

$$\begin{bmatrix}1 & 0\\0 & 0\end{bmatrix} \tag{2.15}$$

This matrix completely eliminates the electric field component along the *y*-axis and leaves the *x* component untouched.

An equally important, and perhaps more interesting, optical component is the wave plate. The wave plate is a component that introduces a phase delay between two orthogonal linear polarization states, and is therefore referred to as a linear retarder. The Jones matrix for a wave plate is given in Equation (2.16). The phase delay, or retardation, is dependent upon the wavenumber *k*, the distance *z* traveled through the material, and the difference in refractive index between the fast and slow axes.

$$\mathbf{J} = \begin{bmatrix}e^{i\Delta\phi/2} & 0\\0 & e^{-i\Delta\phi/2}\end{bmatrix} \tag{2.16}$$

$$\Delta\phi = kz\Delta n \tag{2.17}$$

When the fast and slow axes differ from the defined coordinate system, it is necessary to apply a rotation operation so that the Jones matrix operates upon the eigenvectors of the optical component. This is done using the rotation matrix as shown in Equations (2.18) and (2.19).

$$\mathbf{R}(\theta) = \begin{bmatrix} \cos\theta & -\sin\theta \\ \sin\theta & \cos\theta \end{bmatrix} \tag{2.18}$$

$$\mathbf{J}(\theta) = \mathbf{R}(\theta)\mathbf{J}\mathbf{R}(-\theta) \tag{2.19}$$

Common wave plates are the half-wave and quarter-wave plates which introduce relative phase delays of π and $\pi/2$ respectively. The effect of a half-wave plate is illustrated in Figure 2.2. Light incident at -45° experiences a phase delay of half a wavelength between the *x* and *y* components. The output is a linear polarization state of +45° at the output of the wave plate. This illustrates the effect of the half-wave plate which rotates an input linear polarization state 2θ degrees, where θ is the angle with the fast axis. More intuitively, it can be imagined that the half-wave plate flips the linear polarization about the fast axis. The half-wave plate will also alternate the rotation of circularly polarized light and flip elliptically polarized light.

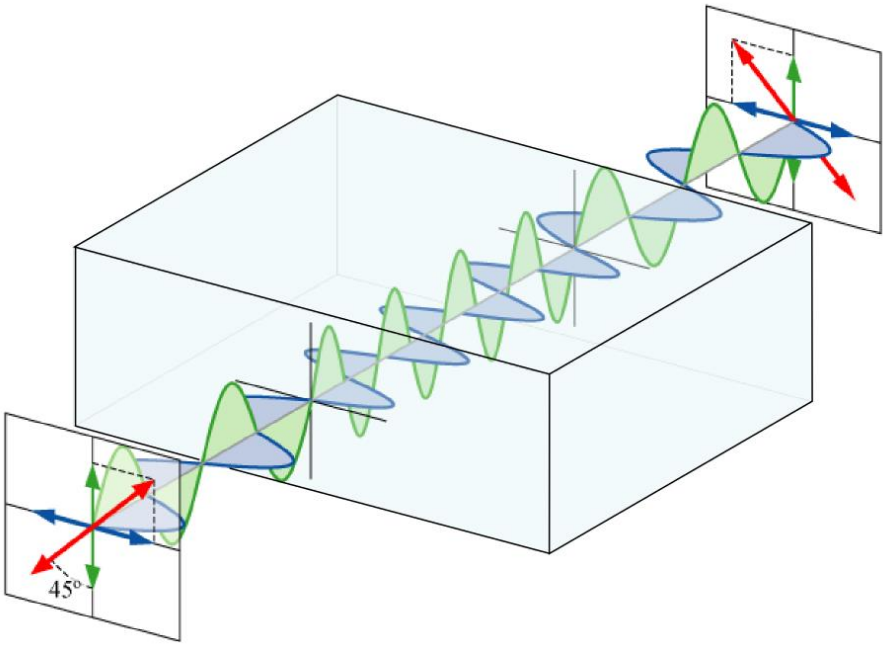

Figure 2.2 Half-wave plate acting upon an input linear polarization. The vertical polarization state is delayed one half-wavelength with respect to the horizontal polarization state, resulting in a flipped polarization state at the output [40].

The quarter-wave plate, which introduces a phase delay of $\pi/2$, can be used to transform linearly polarized light into elliptically or circularly polarized light. To generate circularly polarized light, the components along the fast and slow axis must have equal magnitude. Therefore, from Equation (2.10) we find that linearly polarized light oriented at 45° to the quarter-wave plate will be transformed into circularly polarized light.

Birefringence in a material is a result of a polarization-dependent refractive index [35]. Until this point, we have considered only the real component of the refractive index. Materials may also exhibit polarization-dependent absorption which is contained in the imaginary component of the refractive index. This polarization-dependent absorption is known as diattenuation. The Jones matrix for a material that exhibits diattenuation is given in Equation (2.20). An optical component that behaves in this manner may also be referred to as a partial polarizer.

$$\mathbf{J} = \begin{bmatrix} e^{-\alpha_x} & 0 \\ 0 & e^{-\alpha_y} \end{bmatrix} \tag{2.20}$$

Just as elliptically polarized light represents the most general Jones vector, the elliptical retarder and diattenuator represents the most general Jones matrix. The elliptical retarder has eigenvectors corresponding to elliptically polarized light [41]. This can be seen in the matrix representation.

$$\mathbf{J} = \begin{bmatrix} \cos\theta & -e^{-i\phi}\sin\theta \\ e^{i\phi}\sin\theta & \cos\theta \end{bmatrix} \begin{bmatrix} e^{i\Delta\phi/2-\alpha_1} & 0 \\ 0 & e^{-i\Delta\phi/2-\alpha_2} \end{bmatrix} \begin{bmatrix} \cos\theta & e^{-\phi}\sin\theta \\ -e^{i\phi}\sin\theta & \cos\theta \end{bmatrix} \tag{2.21}$$

Optically active materials are a familiar example of an elliptical retarder. An optically active material has eigenvectors corresponding to right-hand and left-hand circularly polarized light. This is commonly referred to as circular birefringence.

2.3 Stokes vector representation

While Jones calculus is a powerful and useful mathematical tool for working with polarized light in optical systems, it is only able to characterize fully polarized light. An

alternative calculus was derived by Stokes in the nineteenth century that provides a complete description of light polarization [42, 43]. The Stokes vector **S** consists of the four components *I*, *Q*, *U*, and *V*. Equation (2.22) gives an intuitive definition of the Stokes vectors [44]. The component *I* is equal to the total light intensity, *Q* indicates polarization along the horizontal or vertical axes, *U* indicates polarization along the $\pm 45°$ axes, and *V* indicates circular polarization.

$$\mathbf{S} = \begin{bmatrix} I \\ Q \\ U \\ V \end{bmatrix} = \begin{bmatrix} I_{total} \\ I_{0^\circ} - I_{90^\circ} \\ I_{45^\circ} - I_{-45^\circ} \\ I_{right\ circ} - I_{left\ circ} \end{bmatrix} \tag{2.22}$$

Assuming the light is completely polarized, the Jones vector as defined in Equation (2.9) can be used to calculate the components of the Stokes vector. If the light is not completely polarized, an additional term *A* must be included to account for the amplitude of the non-polarized portion of the optical wave.

$$\begin{bmatrix} I \\ Q \\ U \\ V \end{bmatrix} = \begin{bmatrix} A_x^2 + A_y^2 + A^2 \\ A_x^2 - A_y^2 \\ 2A_x A_y \cos\Delta\phi \\ 2A_x A_y \sin\Delta\phi \end{bmatrix} \tag{2.23}$$

It can be seen from Equation (2.23) that if the light is completely polarized, then *A* is equal to zero and $I^2 = Q^2 + U^2 + V^2$. Partially polarized light can be defined by the degree of polarization calculated by Equation (2.24). The degree of polarization *P* may vary between zero and one.

$$P = \frac{\sqrt{\left(Q^2 + U^2 + V^2\right)}}{I} \tag{2.24}$$

The most common way to visualize the Stokes vectors is using a three-dimensional rectangular coordinate system where the coordinates are defined by the Stokes vector components *Q*, *U*, and *V*. The tip of the Stokes vector lies upon what is known as the Poincare sphere. The Poincare sphere provides a convenient visual representation of polarized light and

the effects of birefringent optical components. Along each axis of the coordinate system, the sphere intersects the polarization states associated with that particular Stokes vector component. All other locations on the sphere represent elliptically polarized light. Figure 2.3 shows several polarization states and their corresponding locations on the Poincare sphere. When dealing with partially polarized light it is often useful to plot the normalized Stokes vector calculated by Equation (2.25). The normalized Stokes vector lies on a unit sphere even though the degree of polarization may be less than one.

$$\begin{bmatrix} \hat{Q} & \hat{U} & \hat{V} \end{bmatrix}^{\mathrm{T}} = \frac{\begin{bmatrix} Q & U & V \end{bmatrix}^{\mathrm{T}}}{\sqrt{\left(Q^2 + U^2 + V^2\right)}} \tag{2.25}$$

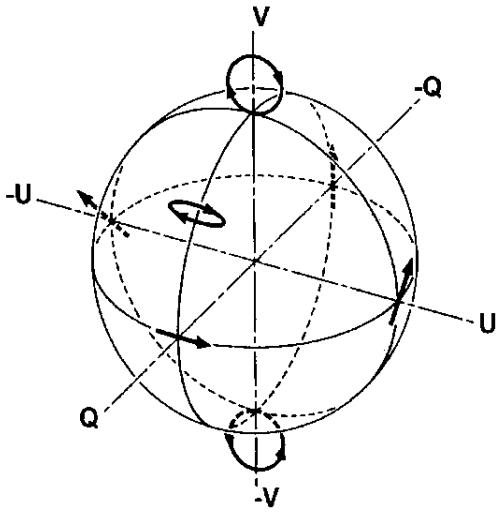

Figure 2.3 The Poincare sphere showing the six particular polarization states corresponding to the Stokes vector components and an additional elliptical polarization state [44].

Just as the Jones matrix operates upon the Jones vector, the Mueller matrix operates upon the Stokes vector. The Mueller matrix is a four-by-four matrix which represents the polarizing, retardation, and de-polarizing effects of an optical element.

$$\mathbf{S}' = \mathbf{M}\mathbf{S}' \tag{2.26}$$

$$\begin{bmatrix} I' \\ Q' \\ U' \\ V' \end{bmatrix} = \begin{bmatrix} M_{11} & M_{12} & M_{13} & M_{14} \\ M_{21} & M_{22} & M_{23} & M_{24} \\ M_{31} & M_{32} & M_{33} & M_{34} \\ M_{41} & M_{42} & M_{43} & M_{44} \end{bmatrix} \begin{bmatrix} I \\ Q \\ U \\ V \end{bmatrix} \tag{2.27}$$

Although it is more difficult to work with, the Mueller matrix is capable of operations that the Jones matrix is not. As an example, consider light with a degree of polarization equal to zero. Passing the light through a polarizer aligned with the horizontal will produce horizontally polarized light with a degree of polarization equal to one, as shown in Equation (2.28).

$$\begin{bmatrix} 1/2 \\ 1/2 \\ 0 \\ 0 \end{bmatrix} = \frac{1}{2}\begin{bmatrix} 1 & 1 & 0 & 0 \\ 1 & 1 & 0 & 0 \\ 0 & 0 & 0 & 0 \\ 0 & 0 & 0 & 0 \end{bmatrix}\begin{bmatrix} 1 \\ 0 \\ 0 \\ 0 \end{bmatrix} \tag{2.28}$$

Standard PS-OCT systems detect fully polarized light [45]. Therefore the Jones matrix is typically sufficient to model PS-OCT imaging.

3 Polarization-Sensitive Optical Coherence Tomography

3.1 Theory and free-space implementation

The goal of PS-OCT is to measure the effect that the sample of interest has upon the light vector. To accomplish this goal, the standard OCT imaging system must be redesigned taking into account the polarization of the light at each point throughout the system. Recall the optical setup described when introducing the Jones calculus in Section 2.2. The optical beam propagates in a single direction with the electric field restricted to the orthogonal plane, as in Equation (2.7). This scenario is applicable when describing the collimated beam in the OCT interferometer. Because OCT operates at relatively low numerical aperture, the same scenario holds true in the imaged sample as well [46]. The imaging beam can then be viewed as a Jones or Stokes vector, and the sample can be viewed as an optical element with a corresponding Jones or Mueller matrix. Any circular birefringence will be negated due to the double-pass through the sample [37, 47]. Therefore, the sample is modeled as a linear retarder with the optic axis fixed in the *Q*-*U* plane of the Poincare sphere.

To explore the birefringence of biological tissue, in 1992, Hee et al. developed a polarization-sensitive optical coherence ranging system [48]. Although it was unable to perform multidimensional imaging, the technological advancements necessary for polarization-sensitive measurements were present in this initial design. The system was used to probe the birefringence of the calf coronary artery. This polarization-sensitive ranging design was extended to two-dimensional imaging in 1997, resulting in the first demonstration of PS-OCT [24]. This initial PS-OCT demonstration imaged tendon, a highly birefringent biological sample. Destruction of the birefringent structure due to laser irradiation was also demonstrated, suggesting that PS-OCT is well suited for investigating early changes in underlying tissue structure, perhaps even earlier than is evident in standard structural OCT. These first PS-OCT results are shown in Figure 3.1.

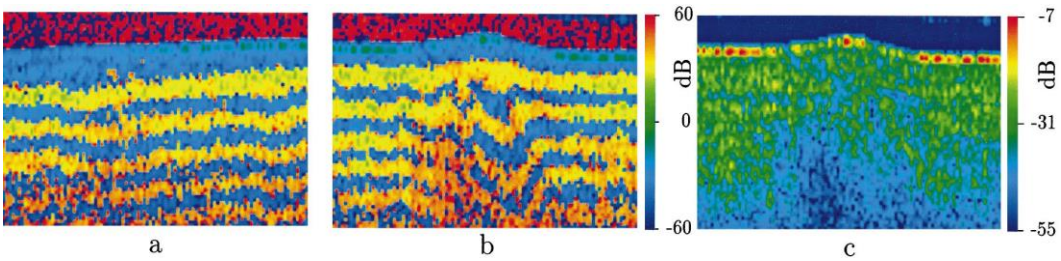

Figure 3.1 The first published PS-OCT images. (a) Birefringence image of healthy bovine tendon. (b) Birefringence image of tendon after laser irradiation causing damage to tissue structure. (c) Reflectance image of damaged tendon [24].

Measuring the vector nature of light in an OCT system requires polarization control in both illumination and detection. To detect the Jones vector, the interference signal must be projected onto two orthogonal basis vectors. This is done using a polarizing beam splitter (PBS). A PBS divides the incident light beam into two orthogonal linear polarization states. These two beams can then be measured to provide the Jones vector. The relative amplitude and phase between the two detected signals determines the polarization state of the detected interference signal. This method of detection is used in nearly all PS-OCT systems [24, 44, 49, 50].

The polarization state of the light incident upon the sample must be chosen carefully to ensure interaction with the birefringence of the sample. To illustrate this fact, consider a sample with a round-trip birefringence modeled by a quarter-wave plate. Illumination with linearly polarized light aligned with either the fast or slow axis will be reflected back in the exact same polarization state. However, illumination with light polarized at ±45° to either axis will return as circularly polarized light. Illumination with linearly polarized light is clearly a poor choice, as interaction with the sample birefringence is entirely dependent upon the orientation of the sample.

To guarantee interaction with the sample birefringence, the illumination light must have a field component along both the slow and fast axes. Circularly polarized light meets this requirement. Regardless of how the sample is rotated, the incident circularly polarized light can always be decomposed into the sum of two orthogonal linear polarization states aligned with the fast and slow axes of the sample. For this reason, circularly polarized light is the ideal choice for illumination of the sample in PS-OCT.

A typical free-space PS-OCT system is shown in Figure 3.2. Light from a broadband source is passed through a linear polarizer aligned with the horizontal axis. A non-polarizing beam splitter is used to separate light into the sample and reference paths. Light in the reference arm passes through a quarter-wave plate oriented at 22.5° to the input polarization. After reflection from the reference mirror the light passes through the quarter-wave plate a second time. The cumulative effect is identical to a single pass through a half-wave plate with the same orientation. The effect of the half-wave plate is to rotate the incident polarization a total of 45°. Light from the reference arm returns to the non-polarizing beam splitter as 45° linearly polarized light with equal power in both horizontal and vertical polarization states, the basis Jones vectors.

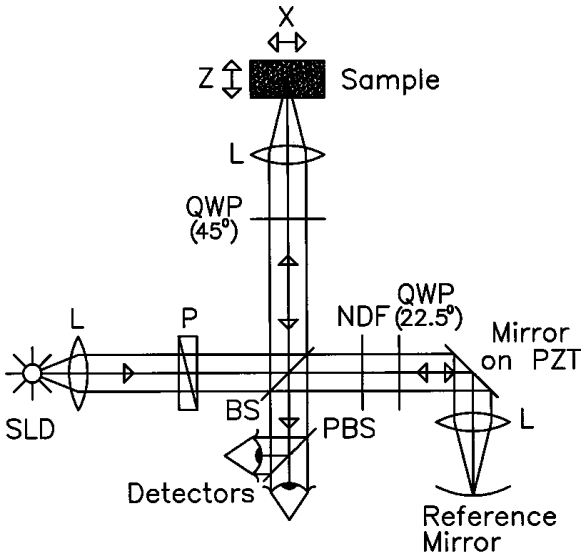

Figure 3.2 Free-space PS-OCT system. SLD: super-luminescent diode, P: polarizer, BS: beam splitter, NDF: neutral density filter, QWP: quarter-wave plate, PZT: piezoelectric transducer, L: lens, PBS: polarizing beam splitter [44].

In the sample arm, the horizontally polarized light passes through a quarter-wave plate oriented at 45° to the horizontal. This produces circularly polarized light incident upon the sample. The birefringence of the sample then alters the polarization state and reflects the light back through the quarter-wave plate to the beam splitter. The result is an unknown elliptical polarization state. Interference with the reference arm light produces a signal projected onto the basis Jones vectors. The interference signal is then split into its orthogonal components by a PBS

and the two components of the Jones vector are detected using standard OCT detection electronics.

$$I = I_R + I_S + 2\,\mathrm{Re}\begin{Bmatrix} \langle E_{R,H} E_{S,H}{}^{*} \rangle \\ \langle E_{R,V} E_{S,V}{}^{*} \rangle \end{Bmatrix} \tag{3.1}$$

The detected interference signal is given by Equation (3.1). To calculate the desired birefringence information about the sample, the relationship between the horizontal and vertical components of the measured signal and the backscattered sample light must be understood. Thankfully, in the free-space design, each component in the PS-OCT interferometer can be modeled using Jones calculus [44, 51]. The linearly polarized input light can be described using the normalized Jones vector in Equation (3.2).

$$\mathbf{E}_{in} = \begin{bmatrix} 1 \\ 0 \end{bmatrix} \tag{3.2}$$

After the double pass through the quarter-wave plate, the reference light at the non-polarizing beam splitter becomes linearly polarized at 45°, as shown in Equations (3.3) and (3.4).

$$\begin{aligned} \mathbf{E}_R &= QWP(22.5°)QWP(22.5°)\mathbf{E}_{in} \\ &= \frac{1}{\sqrt{2}}\begin{bmatrix} 1 \\ 1 \end{bmatrix} \end{aligned} \tag{3.3}$$

$$\mathbf{QWP}\left(25^{\circ}\right) = \mathbf{R}\left(25^{\circ}\right)\begin{bmatrix} e^{i\pi/4} & 0 \\ 0 & e^{-i\pi/4} \end{bmatrix}\mathbf{R}\left(-25^{\circ}\right) \tag{3.4}$$

The sample reflection from depth *z* in the sample is modeled as a wave plate with unknown reflectance *R*, phase retardation δ, and optic axis θ. The corresponding Jones matrix is given by Equation (3.5) where the phase retardation $\delta = kz\Delta n$, as in Section 2.2. Light returning from the sample arm is calculated according as shown in Equation (3.6).

$$\mathbf{S}(z,\delta,\theta) = \mathbf{R}(\theta)\begin{bmatrix} e^{i\delta/2} & 0 \\ 0 & e^{-i\delta/2} \end{bmatrix}\mathbf{R}(-\theta) \tag{3.5}$$

$$\mathbf{E}_S = \mathbf{QWP}(-45°)\mathbf{S}(z,\delta,\theta)\sqrt{R(z)}\mathbf{S}(z,\delta,\theta)\mathbf{QWP}(-45°)\mathbf{E}_{in} \propto \sqrt{R(z)}\begin{bmatrix} e^{i2\theta}\sin\delta \\ \cos\delta \end{bmatrix} \quad (3.6)$$

Following interference with the reference arm light, the measured intensity is given by Equation (3.7).

$$\begin{bmatrix} I_H(z) \\ I_V(z) \end{bmatrix} \propto \begin{bmatrix} R(z)\sin^2\delta \\ R(z)\cos^2\delta \end{bmatrix} \quad (3.7)$$

From this measured signal, the total reflectance and phase retardation values are calculated using Equations (3.8) and (3.9). After computing the inferred complex signal, the optic axis may also be determined using Equation (3.10).

$$I(z) = I_H(z) + I_V(z) \quad (3.8)$$

$$\delta(z) = \tan^{-1}\left\{\sqrt{\frac{I_V(z)}{I_H(z)}}\right\} = kz\Delta n \quad (3.9)$$

$$\theta = \frac{\left(180^\circ - \left(\Delta\phi_H - \Delta\phi_V\right)\right)}{2} \quad (3.10)$$

3.2 Polarization-maintaining fiber implementations

While the free-space design performs well in a laboratory setting, a more flexible approach is needed for the portable imaging systems used in most clinical applications. Standard OCT systems are able to accomplish this goal using single-mode (SM) fiber-based components to replace the free-space optics. However, SM fiber is problematic when used in PS-OCT systems. Ellipticity in the fiber core, external physical stress, and temperature fluctuations all change the effective Jones matrix of the optical fiber [52, 53]. This makes a mathematical analysis of the system quite difficult as the Jones matrix of the optical fiber is both unknown and changing.

A solution to this problem is to use polarization-maintaining (PM) fiber [54-56]. Polarization maintaining fiber is specifically designed to propagate two linear polarization states without crosstalk between the two states. These independent linear polarizations travel along a fast and slow axis as in a typical birefringent material. The ability of the PM fiber to maintain the

polarization state of the light allows the same system design described in Section 3.1 to be used, along with all the benefits of a fiber-based system. A spectral domain PS-OCT system designed using PM fibers is illustrated in Figure 3.3. Note that this design is essentially identical to Figure 3.2, with the main difference being the use of PM fiber.

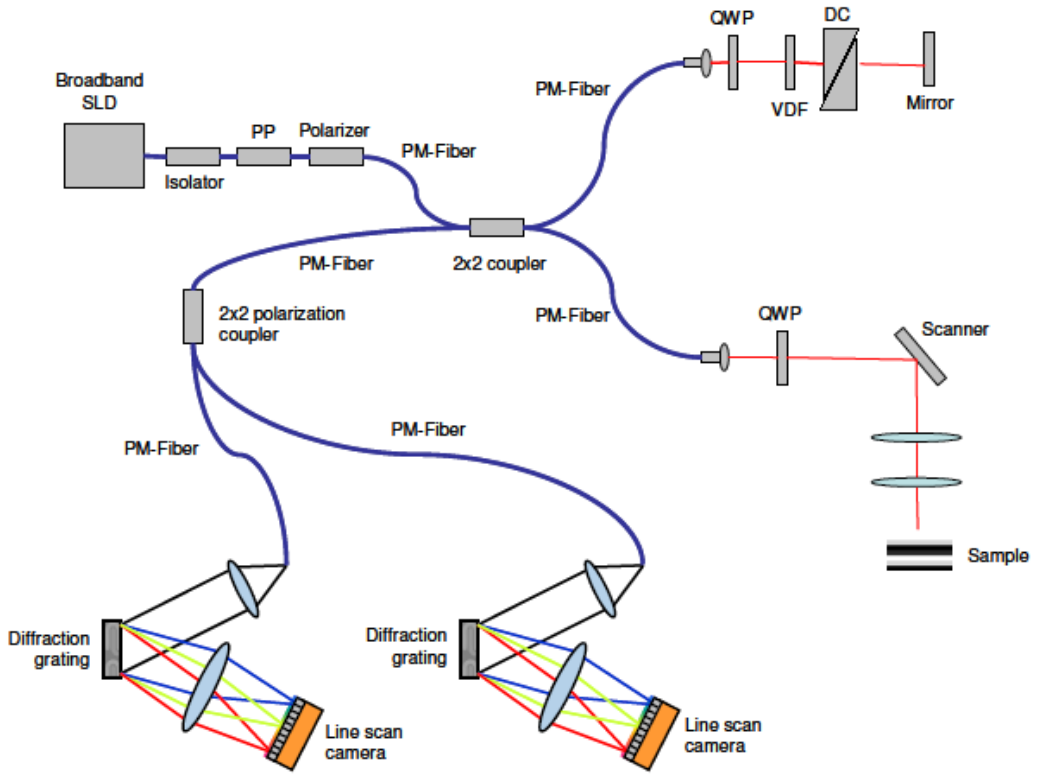

Figure 3.3 PS-OCT system based on PM fiber. SLD: super-luminescent diode, PP: polarization control paddle, PM-Fiber: polarization-maintaining fiber, QWP: quarter-wave plate, VDF: variable density filter, DC: dispersion compensation [55].

It is important to note that due to the birefringent nature of the PM fiber, light travels along the fast and slow axes of the fiber at different speeds. If the lengths of PM fiber in the sample and reference arm are not perfectly matched, the interferograms of the horizontal and vertical channels will be slightly shifted with respect to one another. This can be compensated for physically by using birefringent plates in one of the arms [54], or computationally in post-processing [55].

If this design is used in a portable system where the fibers will be experiencing changing external stresses, such as in a catheter or hand-held design, the optic axis calculation will become

distorted. Therefore a reference reflector such as a coverslip at the exit of the sample fiber must be used for calibration to maintain absolute axis orientation. However, a relative optic axis measurement may be sufficient for many applications. Additionally, bending of the PM fiber does not affect the phase retardation measurement which is the most significant parameter in most applications.

3.3 Jones matrix single-mode fiber implementations

Although PM fiber designs have been successful at extending the original PS-OCT designs into potentially portable designs, SM fiber still has several qualities that make it very desirable to use. SM fiber is typically much cheaper than PM fiber, which is of great importance when building low-cost commercial systems. Additionally, the bandwidth of PM components such as couplers and circulators is significantly lower than that of SM components. This leads to decreased imaging bandwidth and therefore degraded axial resolution. Because of these factors, SM fiber systems may sometimes be preferred.

Single-mode fiber exhibits significant birefringence and can be modeled as a succession of wave plates with random axis orientation, or equivalently a single elliptical retarder with an unknown optic axis [41]. The properties of this elliptical retarder change as the physical conditions experienced by the fiber change. It is not possible to know the Jones matrix of the SM fiber *a priori*, therefore the analysis performed in Sections 3.1 and 3.2 cannot be applied. A useful property of SM fiber is that orthogonal polarization states entering the fiber will remain orthogonal upon exiting the fiber [53, 57]. For example, consider two linear polarization states that are orthogonal to one another upon entering the fiber. Upon exiting the fiber, these two states will have been transformed by the fiber birefringence into arbitrary elliptical polarizations. However, these two elliptical polarizations will be orthogonal to one another. Using this information, the sample birefringence can still be measured even though the actual polarization states may be unknown.

Determining sample birefringence by successive illumination with two orthogonal polarization states is referred to by various names including Jones matrix imaging, Jones method, and Jones analysis. Jones matrix PS-OCT obtains two polarization-diverse measurements at each A-scan location. These measurements correspond to illumination by two orthogonal input polarization states. This information is then used to build up a Jones matrix of the complete imaging system, including the sample [50, 58-60]. Consider a system where the two orthogonal input states are chosen to be horizontally and vertically polarized light, as in [50]. Then the two resulting measurements are given by Equations (3.11) and (3.12), where **J** is the cumulative Jones matrix of the total path through the system and sample.

$$\mathbf{E}_{meas,1} = \begin{bmatrix} H_1 \\ V_1 \end{bmatrix} = \begin{bmatrix} J_{11} & J_{12} \\ J_{21} & J_{22} \end{bmatrix} \begin{bmatrix} 1 \\ 0 \end{bmatrix} = \mathbf{J}\mathbf{E}_{in,1} \tag{3.11}$$

$$\mathbf{E}_{meas,2} = \begin{bmatrix} H_2 \\ V_2 \end{bmatrix} = \begin{bmatrix} J_{11} & J_{12} \\ J_{21} & J_{22} \end{bmatrix} \begin{bmatrix} 0 \\ 1 \end{bmatrix} = \mathbf{J}\mathbf{E}_{in,2} \tag{3.12}$$

The two measured Jones vectors contain the values of the total Jones matrix. This matrix is defined by Equation (3.13).

$$\mathbf{J}_{meas} = \begin{bmatrix} H_1 & H_2 \\ V_1 & V_2 \end{bmatrix} = \mathbf{J}_{out}\mathbf{J}_{sample}\mathbf{J}_{in} \tag{3.13}$$

where $\mathbf{J}_{in}$ represents the fiber path to the sample, $\mathbf{J}_{sample}$ represents the round-trip path through the sample, and $\mathbf{J}_{out}$ represents the fiber path to the detectors. While $\mathbf{J}_{in}$ and $\mathbf{J}_{out}$ were known in the free-space and PM fiber systems, here they are unknown. The measurement from the surface of the sample $\mathbf{J}_{surf}$ can be used to remove the effects of the SM fiber, resulting in a calibrated measurement $\hat{\mathbf{J}}_{meas}$.

$$\mathbf{J}_{surf} = \mathbf{J}_{out}\mathbf{J}_{in} \tag{3.14}$$

$$\begin{aligned} \hat{\mathbf{J}}_{meas} &= \mathbf{J}_{meas}\mathbf{J}_{surf}^{-1} \\ &= \mathbf{J}_{out}\mathbf{J}_{sample}\mathbf{J}_{in}\left(\mathbf{J}_{out}\mathbf{J}_{in}\right)^{-1} \\ &= \mathbf{J}_{out}\mathbf{J}_{sample}\mathbf{J}_{out}^{-1} \end{aligned} \tag{3.15}$$

The output fiber path is modeled as an elliptical retarder with no diattenuation (see Section 2.2). The elliptical retarder is a unitary matrix [37, 59]. Therefore, $\hat{\mathbf{J}}_{meas}$ is a similarity transformation of $\mathbf{J}_{sample}$, where $\mathbf{J}_U$ is a unitary matrix. The similarity transformation preserves the eigenvectors of the sample Jones matrix λ_1 and λ_2, allowing the phase retardation to be obtained by Equation (3.17). Note that the matrix $\mathbf{J}_{out}$ is still unknown. Because of this, additional calibration hardware is needed to extract an absolute optic axis orientation [61].

$$\hat{\mathbf{J}}_{meas} = \mathbf{J}_U \begin{pmatrix} e^{i\delta/2} & 0 \\ 0 & e^{-i\delta/2} \end{pmatrix} \mathbf{J}_U^{-1} \tag{3.16}$$

$$\delta = \tan^{-1}\left[\frac{\mathrm{Im}\left(\lambda_1 / \lambda_2 \right)}{\mathrm{Re}\left(\lambda_1 / \lambda_2 \right)} \right] \tag{3.17}$$

Although Jones matrix imaging has been performed using numerous different system designs, these systems can be divided into two broad categories based on how the modulation of the input polarization is performed. Initial designs used active polarization modulation to illuminate with alternating orthogonal polarization states. The first fiber-based Jones matrix PS-OCT system is shown in Figure 3.4. A polarization modulator is used to actively switch the input polarization state between successive A-scans. Two A-scans are taken at each imaging location to build up the Jones matrix. This causes a factor of two decrease in the maximum line rate of the system. This is a significant drawback, as higher line rates are necessary for *in vivo* volumetric imaging. Polarization modulators are typically quite expensive and non-trivial to calibrate. This adds significant complexity and financial cost to the system.

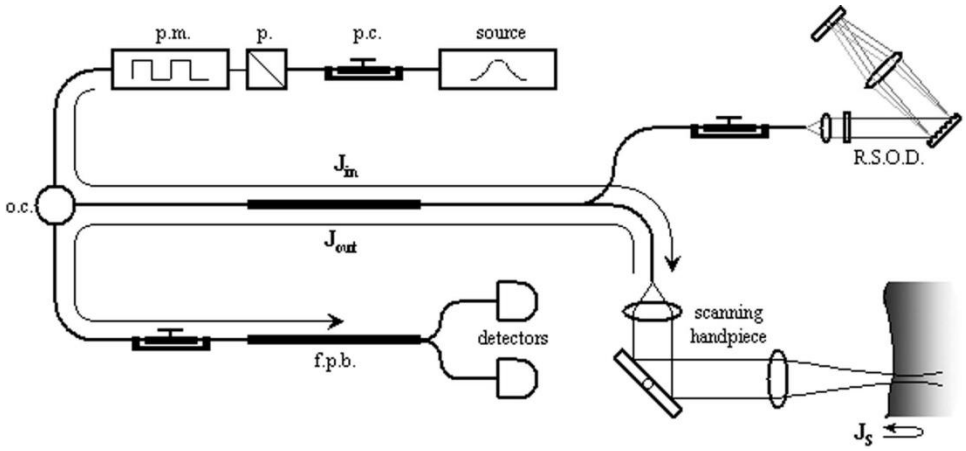

Figure 3.4 Jones matrix PS-OCT system using active polarization modulation. p.c. polarization controller, p. linear polarizer, p.m. polarization modulator, o.c. optical circulator, R.S.O.D. rapid scanning optical delay, f.p.b. fiber-based polarizing beam splitter [59].

A recently developed alternative method is to modulate the input polarization state using passive optical components [50]. An illustration of perhaps the most recent SM fiber-based PS-OCT design is shown in Figure 3.5. The design uses a Mach-Zehnder interferometer to completely separate the sample and reference arms for independent polarization control.

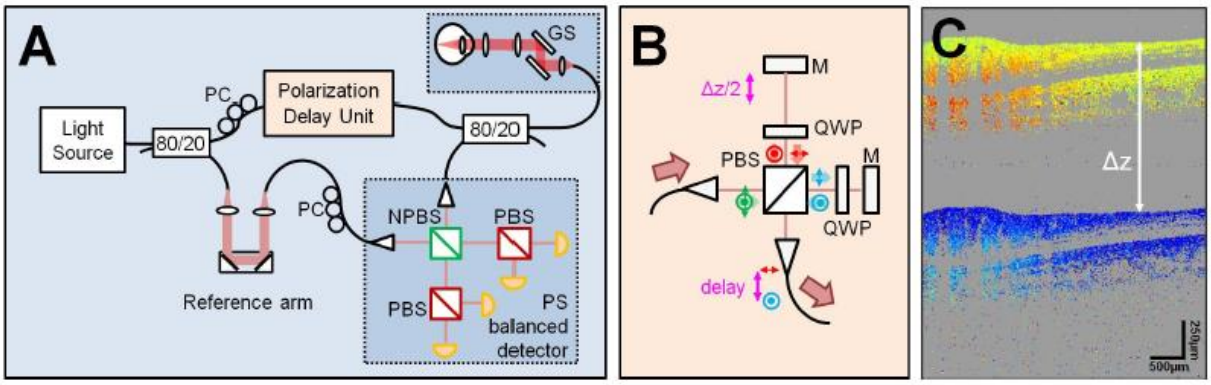

Figure 3.5 Jones matrix PS-OCT system using passive polarization modulation. (A) System diagram. PC: polarization controller, GS: galvo scanners, NPBS: non-polarizing beam splitter, PBS: polarizing beam splitter. (B) Layout of polarization delay unit. QWP: quarter-wave plate, M: mirror. (C) Single B-scan from one of the balanced detectors. The two measurements resulting from the orthogonal illumination states are detected simultaneously [50].

The novelty of this system lies in the polarization delay unit shown in Figure 3.5 B. A polarizing beam splitter separates the source power into two orthogonal polarization states. Each polarization state then passes through a quarter-wave plate and is reflected back toward the PBS by a mirror. The round-trip through the quarter-wave plate alternates the polarization state ensuring that light exits the unit through the fourth side of the PBS. The length of one arm is set to be longer than the other. This can be adjusted to provide a small delay between the two

polarization states exiting the unit. The result is that the sample arm appears longer for one of the polarization states. This will cause the imaged sample to appear further away when illuminated with that particular state.

A reconstructed B-scan from one of the detectors is shown in Figure 3.5 C. Due to the long instantaneous coherence length of the swept-source laser, the system has a large usable imaging range. Therefore it is possible for measurements from both illuminations to be taken in a single image. The offset Δz between the two illuminations must be greater than the imaging depth into tissue, yet small enough to ensure that the tissue remains within the imaging depth. The two measurements are separated and aligned in post-processing based upon the known distance Δz. Standard Jones matrix processing can then be applied. A similar design has been reported using a free-space spectrometer setup. This design uses full-range OCT to increase the usable imaging range so that two measurements of the tissue may be made simultaneously [62]. The passive modulation design removes the need for expensive and complicated modulators and allows the imaging system to operate at its maximum speed. As a result, it has become the preferred method for Jones matrix imaging.

3.4 Alternative single-mode fiber implementations

When a relative phase retardation measurement is acceptable, simpler system designs can be used. In this case it is not necessary to mathematically remove the retardation effects of the SM fiber. This relative phase information is suitable for both research and commercial purposes. Relative phase information has been used to image birefringent muscle samples and scattering phantoms to investigate the effects of multiple scattering upon polarization uniformity [45]. Additionally, a commercial swept-source PS-OCT system sold by Thorlabs, Inc. uses SM fiber to acquire relative phase retardation information [63, 64]. An illustration of the system design is shown in Figure 3.6.

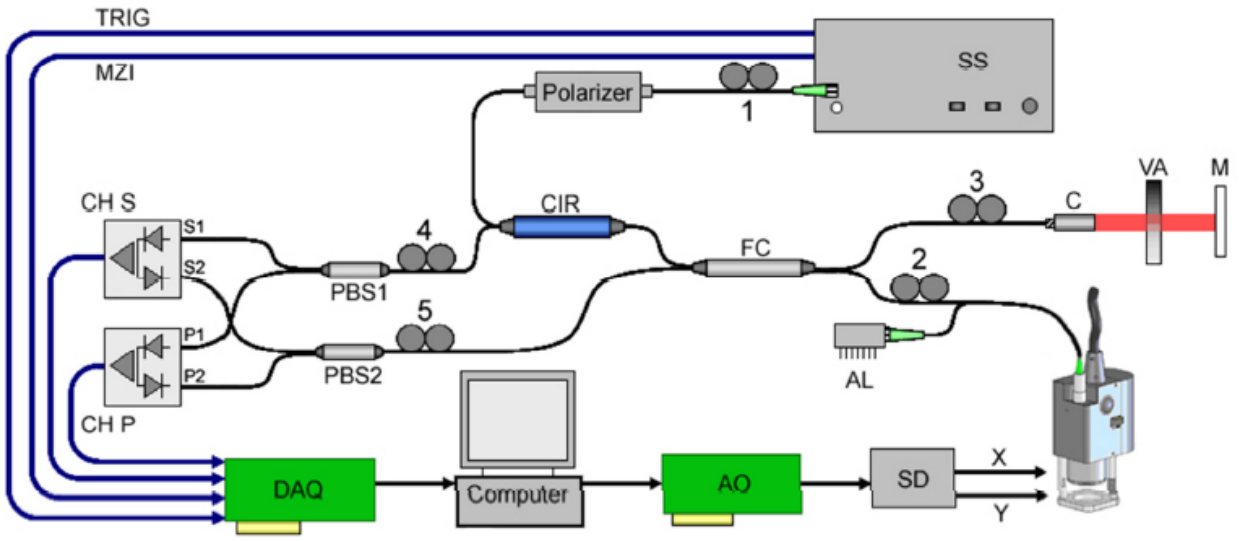

Figure 3.6 Thorlabs PSOCT-1300 system diagram. SS: swept-source, CIR: circulator, FC: fiber coupler, C: collimator, VA: variable attenuator, M: mirror, AL: aiming laser, PBS: polarizing beam splitter [63].

From this diagram it can be seen that the sample is illuminated by a single arbitrary polarization state. Therefore, it is possible that the sample birefringence may not be detected. A polarization control paddle is provided in the sample arm to allow the polarization to be changed, resulting in the drastically different images seen in Figure 3.7. The paddles must therefore be adjusted to optimize the birefringence seen in each sample. This is also true of the setup in [45]. As a result, comparison of birefringence data between different imaging samples in different imaging sessions becomes quite uncertain. The design used in this thesis will address this issue. A complete explanation of the system is given in Chapter 4.

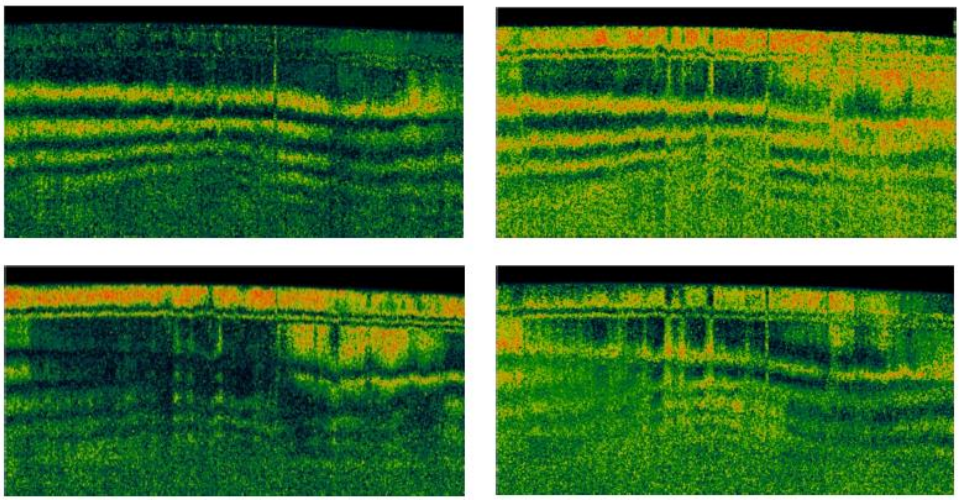

Figure 3.7 Images of a birefringent sample with different incident polarization states. The birefringence measurement is clearly greatly affected by the polarization state [63].

4 Swept-Source PS-OCT Implementation

4.1 Fourier domain mode-locked laser

The swept-source laser used in this thesis is the Fourier domain mode-locked laser (FDML). The FDML is a high-speed swept-source laser designed in 2006 specifically for use in OCT imaging [28]. High-speed imaging helps alleviate the effects of motion artifacts during imaging and is a requirement in point-of-care and intraoperative applications. Standard tunable lasers operate by rapidly sweeping the passband of an optical filter inside the resonator. Because only a single wavelength is allowed to resonate at any given time, each new wavelength must build up from spontaneous emission before lasing. In contrast, the FDML allows all of the tunable wavelengths to resonate continually in the cavity. This is achieved using a dispersion managed delay line. Dispersion in the delay line is optimized so that the cavity round-trip time is the same for all tunable wavelengths. The optical filter passband then oscillates with a frequency equal to multiples of the cavity round-trip frequency. This causes each wavelength to return to the filter at the precise time when it is allowed to pass. The result is a higher sweep speed without sacrificing output power. Figure 4.1 is an illustration of this concept.

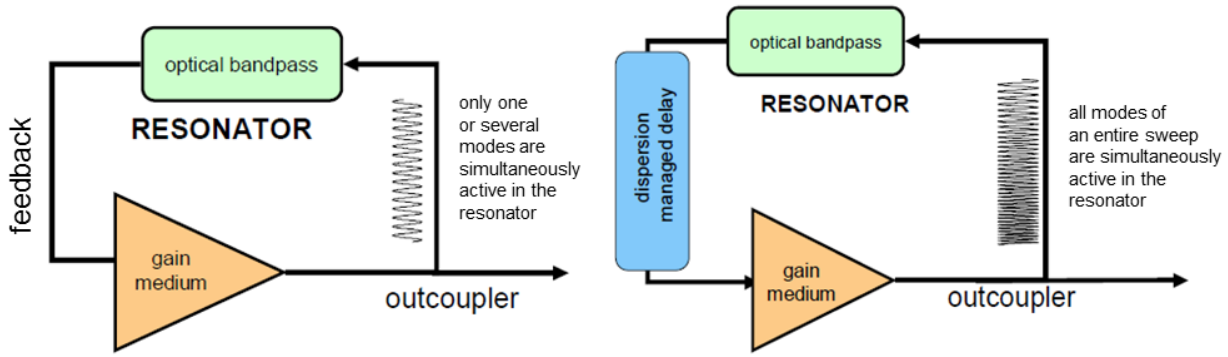

Figure 4.1 Standard tunable laser (left) compared with the FDML (right). Adapted from [28].

The FDML schematic shown in Figure 4.2 mirrors the conceptual design of Figure 4.1. The optical filter is a tunable fiber Fabry-Perot (FFP), which behaves according to Equation (4.1)

.

$$nl = \frac{\lambda}{4} m, \quad m = 1, 2, 3, \ldots \tag{4.1}$$

The optical path length of the filter is equal to the physical length l multiplied by the index of refraction n. By stretching and compressing the filter length, a wide range of wavelengths λ are allowed to pass. The FFP length, and therefore the output wavelength, is controlled using a function generator. A DC voltage is used to set the central wavelength of the filter. A sinusoidal voltage is applied to sweep the wavelength over the bandwidth of the gain medium. This results in a swept-source laser output which oscillates over the desired wavelength range.

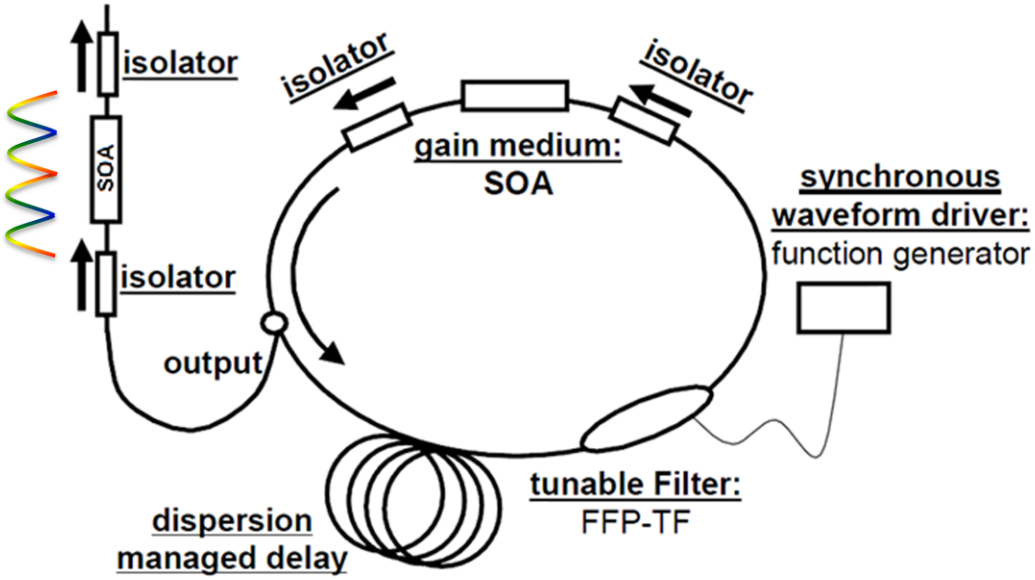

Figure 4.2 FDML laser design. The output oscillates between long and short wavelengths. SOA: semiconductor optical amplifier, FFP-TF: fiber Fabry-Perot tunable filter. Adapted from [28].

The FDML output alternates between forward sweeps (short-to-long wavelengths) and backward sweeps (long-to-short wavelengths). It is more desirable to have unidirectional wavelength sweeps. This can be accomplished without sacrificing speed by using a buffering stage [65]. The backward sweep typically has a lower noise floor, and therefore is chosen as the unidirectional sweep.

The first goal is to remove the forward sweep. This is done by modulating the laser driver to turn off during the forward sweep. The second step is to create a copy of the backward sweep to replace the missing forward sweep. Light is coupled out at a second location halfway through

the cavity so that it exits when the forward sweep would normally be occurring. The two outputs are then coupled together creating a series of unidirectional sweeps at the full sweep rate.

Buffering stages can also be used to increase the sweep rate of the laser beyond the frequency range of the FFP. This thesis uses the FDML in the double-buffered setup as illustrated in Figure 4.3. In double-buffered operation, the laser is driven to generate a backward sweep in one-quarter of the cavity round-trip time. Two copies of the sweep are coupled out of the cavity and combined at coupler C3 as in the single-buffered case. These sweeps are then copied and delayed one-quarter of the cavity round-trip time. After recombining at coupler C4, there is a total of four backward sweeps. Using buffered operation, a forward and backward sweep have been replaced with four consecutive backward sweeps.

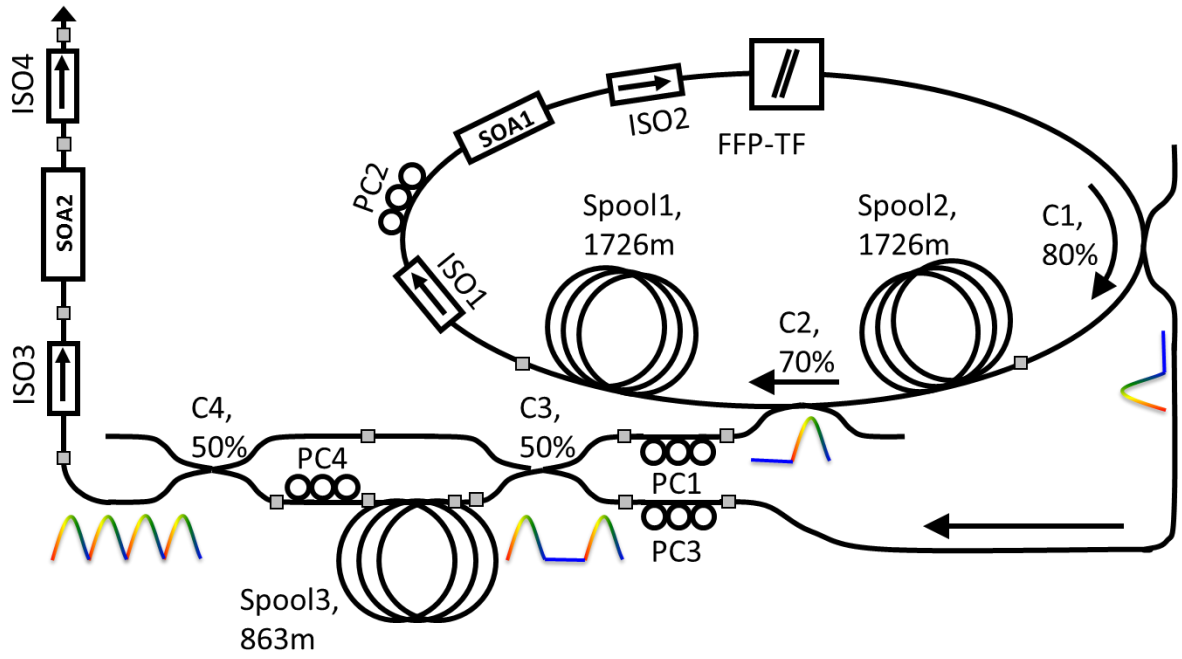

Figure 4.3 Double-buffered FDML schematic. Copies of the backward sweep are delayed and combined to increase the effective sweep rate. ISO: isolator, SOA: semiconductor optical amplifier, PC: polarization controller, C: coupler, FFP-TF: fiber Fabry-Perot tunable filter. Adapted from [66].

The laser operates at a central wavelength of 1310 nm. Dispersion in the cavity was managed using SMF-28e fiber which has zero dispersion at 1313 nm and a negligible dispersion slope of 0.086 ps/km/nm^2. The group refractive index of the fiber is 1.46 at 1310 nm.

$$\text{cavity rate} = \frac{c}{nl} \tag{4.2}$$

The cavity rate is determined by Equation (4.2), and was experimentally found to be 58.9 kHz. Using the double-buffered setup, backward sweeps are generated at 235.6 kHz. The −3 dB bandwidth of the FDML is approximately 122.5 nm, corresponding to a theoretical axial resolution of 6.2 μm in air. Due to loss of bandwidth in the fiber components, the experimental axial resolution of the complete PS-OCT system is measured to be 9.9 μm, or 7 μm in tissue assuming refractive index of 1.4. The FDML driving signals and the resulting sweep pattern are shown in Figure 4.4. The fringe pattern shown is the output of a fixed-length interferometer.

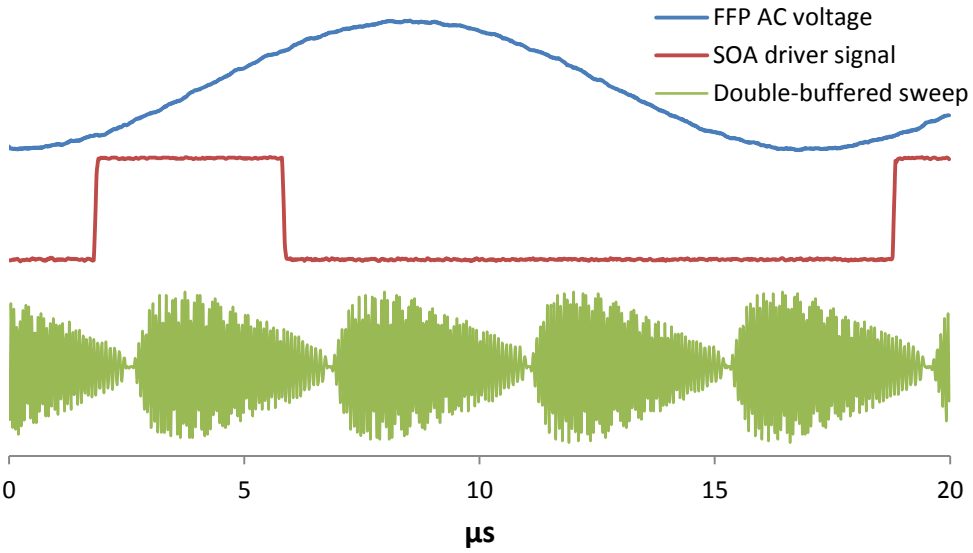

Figure 4.4 Operation of the double-buffered FDML. The driver allows lasing for a quarter of the round-trip time. The backward sweep is then copied using buffering stages to generate four backward sweeps. FFP: fiber Fabry-Perot, SOA: semiconductor optical amplifier.

4.2 Polarization-sensitive interferometer design

To use the FDML in phase sensitive applications it is necessary to implement a calibration arm for resampling and triggering purposes. The swept-source output is typically chirped and must be resampled to be linear in wavenumber. At the beginning of each imaging session, a calibration scan is acquired. The calibration scan is generated using a fixed-length Mach-

Zehnder interferometer (MZI), shown in Figure 4.5. The scan is then processed to determine the correct resampling parameters for linearization.

Each sweep of the laser corresponds to a single A-line in the OCT dataset. It is desirable to have a trigger signal for the acquisition of each line. Additionally, instability in the phase of the sweep leads to phase variations between A-lines. A fiber Bragg grating (FBG) can be used as a phase stable trigger signal [50, 67, 68]. The FBG strongly reflects a very narrow bandwidth of light. In the configuration shown in Figure 4.5, the reflection from the FBG generates a trigger at precisely the same wavelength in each sweep. A custom designed FBG at 1377.4 ±0.1 nm was used. Figure 4.6 shows both the MZI calibration signal and the line trigger reflected from the FBG.

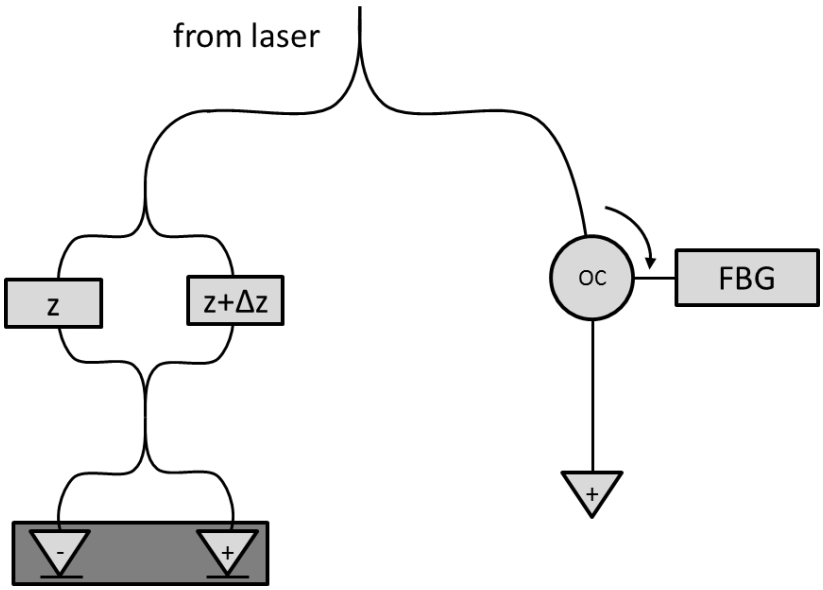

Figure 4.5 Calibration arm. Left path is the fixed-length interferometer for generating calibration fringes. The right path generates the phase stable line trigger. OC: optical circulator, FBG: fiber Bragg grating.

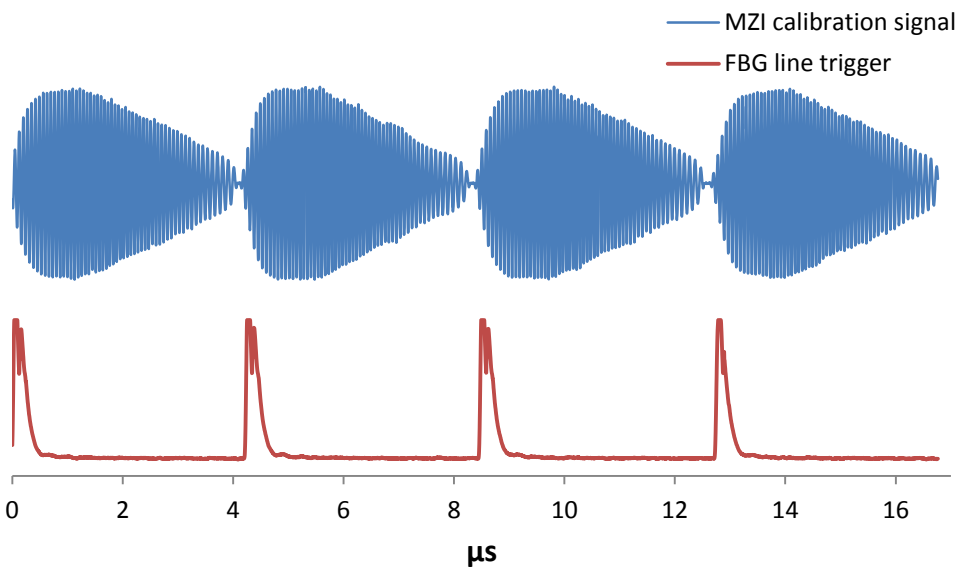

Figure 4.6 Output of the calibration arm. MZI: Mach-Zehnder interferometer, FBG: fiber Bragg grating.

The polarization-sensitive interferometer designed for this thesis uses SM fiber and is similar to the imaging systems discussed in Section 3.4. The design has been modified from a circulator-based Michelson setup to a coupler-based Mach-Zehnder design, mimicking the setup found in Figure 3.5. This eliminates the polarization mode dispersion and wavelength-dependent polarization effects of the circulators. At high line rates, the addition of the circulator fiber length into one detection path can cause the dual-balanced detection to fail. The Mach-Zehnder design eliminates this problem as well.

A schematic of the system is shown in Figure 4.7. As light enters the interferometer, it passes through a fiber-based linear polarizer to ensure that the entire bandwidth is completely polarized along the same direction. Light in the reference arm is calibrated using polarization controllers to provide equal power in both of the output polarization states. Therefore any difference in intensity between the two channels will be due to the sample response.

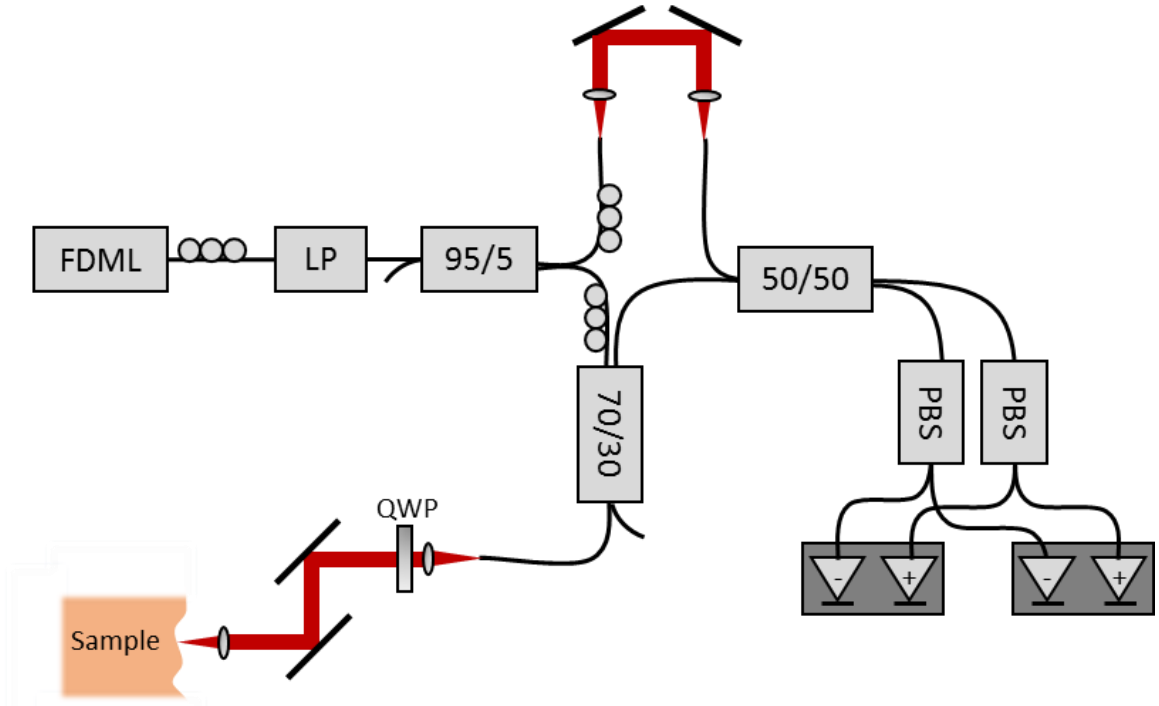

Figure 4.7 PS-OCT interferometer. FDML: Fourier-domain mode-locked laser, LP: linear-polarizer, QWP: quarter-wave plate, PBS: polarizing beam splitter.

As discussed in Section 3.1, circularly polarized light incident upon the sample is preferred to guarantee interaction with the sample birefringence. The single mode fiber designs used in [45, 63, 64] do not enforce this condition. Because of this limitation, they require that the polarization in the sample arm be adjusted to optimize the response from each tissue sample. This makes studies of multiple samples over several imaging sessions prone to error. To correct this issue, this thesis uses a calibration procedure to enforce circularly polarized sample illumination. While the use of SM fiber in the system still results in a relative phase retardation measurement, sample birefringence will be detected.

For the quarter-wave plate in the sample arm to generate circularly polarized light, it must be illuminated with linearly polarized light at 45° to the fast and slow axes. The polarization controllers in the sample arm must be adjusted so that light exiting the fiber meets this condition. To find the proper orientation, a free-space linear polarizer is inserted prior to the wave plate using a flip mount. A mirror is used as the calibration sample. The axis of the polarizer is rotated until no light returns from the sample arm, regardless of the polarization controller orientation.

The polarizer is then correctly aligned. This is explained by Equation (4.3), where the polarizer Jones matrix is designated by **P**.

$$\begin{aligned}\mathbf{E}_{s,out} &= \mathbf{P}\left(0^\circ\right)\mathbf{QWP}\left(45^\circ\right)\mathbf{QWP}\left(45^\circ\right)\mathbf{P}\left(0^\circ\right)\mathbf{E}_{s,in} \\ &= \mathbf{P}\left(0^\circ\right)\mathbf{R}\left(45^\circ\right)\begin{bmatrix} e^{i\pi/2} & 0 \\ 0 & e^{-i\pi/2} \end{bmatrix}\mathbf{R}\left(-45^\circ\right)\begin{bmatrix} 1 \\ 0 \end{bmatrix} \\ &= \begin{bmatrix} 1 & 0 \\ 0 & 0 \end{bmatrix}\begin{bmatrix} 0 \\ 1 \end{bmatrix} \\ &= \begin{bmatrix} 0 \\ 0 \end{bmatrix}\end{aligned} \tag{4.3}$$

Once the linear polarizer is aligned, the quarter-wave plate is removed from the sample arm path using a flip mount. The sample arm polarization controllers are then adjusted until no power returns. The light exiting the sample arm fiber is then entirely orthogonal to the axis of the linear polarizer and aligned at 45° to the fast and slow axes of the quarter-wave plate. The linear polarizer is then removed from the sample arm, and the quarter-wave plate is returned for imaging. A summary of the calibration procedure is given below:

1. Remove the fibers from the "-" ports of the dual-balanced detectors.
2. Adjust the polarization of the FDML output to maximize power through the linear polarizer.
3. Block the reference arm and place a mirror in the sample arm.
4. Insert the linear polarizer prior to the quarter-wave plate into the sample arm. Adjust the linear polarizer until no power returns from the mirror, regardless of the incident polarization.
5. Remove the quarter-wave plate. Adjust the incident polarization until no power returns from the mirror.
6. Return the quarter-wave plate to the sample arm. Remove the linear polarizer.
7. Block the sample arm and unblock the reference arm.
8. Adjust the reference arm polarization until the two output polarizations are equal.

9. Return the fibers to the "-" ports of the dual-balanced detectors.
10. Adjust the polarization of the "-" ports until the measured polarizations are equal.

The interference pattern is measured using two Thorlabs PDB-1300 350 MHz dual-balanced photodetectors. Each channel is then digitized at 250 MS/s using an AlazarTech ATS9350 data acquisition (DAQ) board for a total acquisition rate of 500 MS/s. This sampling rate gives an optical imaging depth of approximately 3.45 mm. The sensitivity was measured by first placing a mirror in the focus of the sample arm and attenuating the power with a neutral density filter to avoid saturation. Comparing the OCT signal near zero optical path length difference with the noise floor and correcting for attenuation resulted in a system sensitivity of 95 dB. The reference arm was then adjusted over several millimeters. The resulting intensity roll-off was 1.1 dB/mm.

Both the structural OCT information and the polarization-sensitive information can be calculated from the acquired data. After performing a Fourier transform to the spatial domain, both the magnitude and phase are available for each point in the image. The detected polarization states are designated *H* and *V*. The total magnitude of the reflected signal *R* and the phase retardation δ are calculated using Equations (4.4) and (4.5), respectively. Note that due to the arbitrary change in polarization induced by the SM fiber, the measured phase retardation is relative. However, the relationship between polarization states within the image is accurate due to the calibration techniques.

$$R = \sqrt{|H|^2 + |V|^2} \tag{4.4}$$

$$\delta = \text{angle}\left(H \times V^*\right) \tag{4.5}$$

The analog output from a data acquisition board (National Instruments PCIe-6353) controls the positioning of galvanometer mirrors (Cambridge Technology) to scan the beam in the transverse plane, providing three-dimensional volumetric imaging. A 40 mm focal length lens is used to focus the beam. The numerical aperture (NA) is 0.07, resulting in a transverse resolution of 9 μm. The final 15% of the scanning waveform is used to allow the galvanometer

to return to its initial position. At the standard 1024 A-scans per frame, this corresponds to a scan rate of approximately 194 frames per second.

A custom LabVIEW interface was developed to allow user control of the data acquisition parameters. Settings for both the galvanometer waveforms and the data acquisition are adjustable, including scan range and samples per A-scan. Typically a maximum of 960 samples of the interferogram are acquired per A-scan to ensure that no line triggers are missed. The number of A-scans per frame and frames per volume are also selectable. The selectable parameters are exported to a .xml file along with user notes for future reference. A screen capture of the LabVIEW interface is shown in Figure 4.8. All acquisition, processing, and display is performed using dynamic-link library (DLL) functions written in the C programming language. Relevant user settings are passed to the C functions via the LabVIEW Call Library Function node.

4.3 GPU processing and display

The high line rate of the double-buffered FDML is well-suited for applications such as hand-held imaging. However, to be useful in an intraoperative or clinical setting the data must also be processed and displayed in real-time. Processing at these high data rates is challenging even for standard OCT processing. Successful high-speed processing solutions include both the digital-signal processor (DSP) [69] and the graphics processing unit (GPU) [70]. The DSP is useful for developing point-of-care embedded systems devices that are concerned with low power consumption, low cost, and a small footprint. Both OCT and more complex optical tomography algorithms such as Doppler and interferometric synthetic aperture microscopy (ISAM) have been successfully implemented using DSPs [69, 71-73].

If a cart-based system is desirable, as in intraoperative applications, then GPUs are preferred due to the higher processing speed and ease of integration with PC-based systems. An additional advantage of the GPU is direct access to the PC display. Real-time processing and

display of OCT data has been performed using GPUs [70, 74]. Doppler and ISAM have also been demonstrated [75, 76].

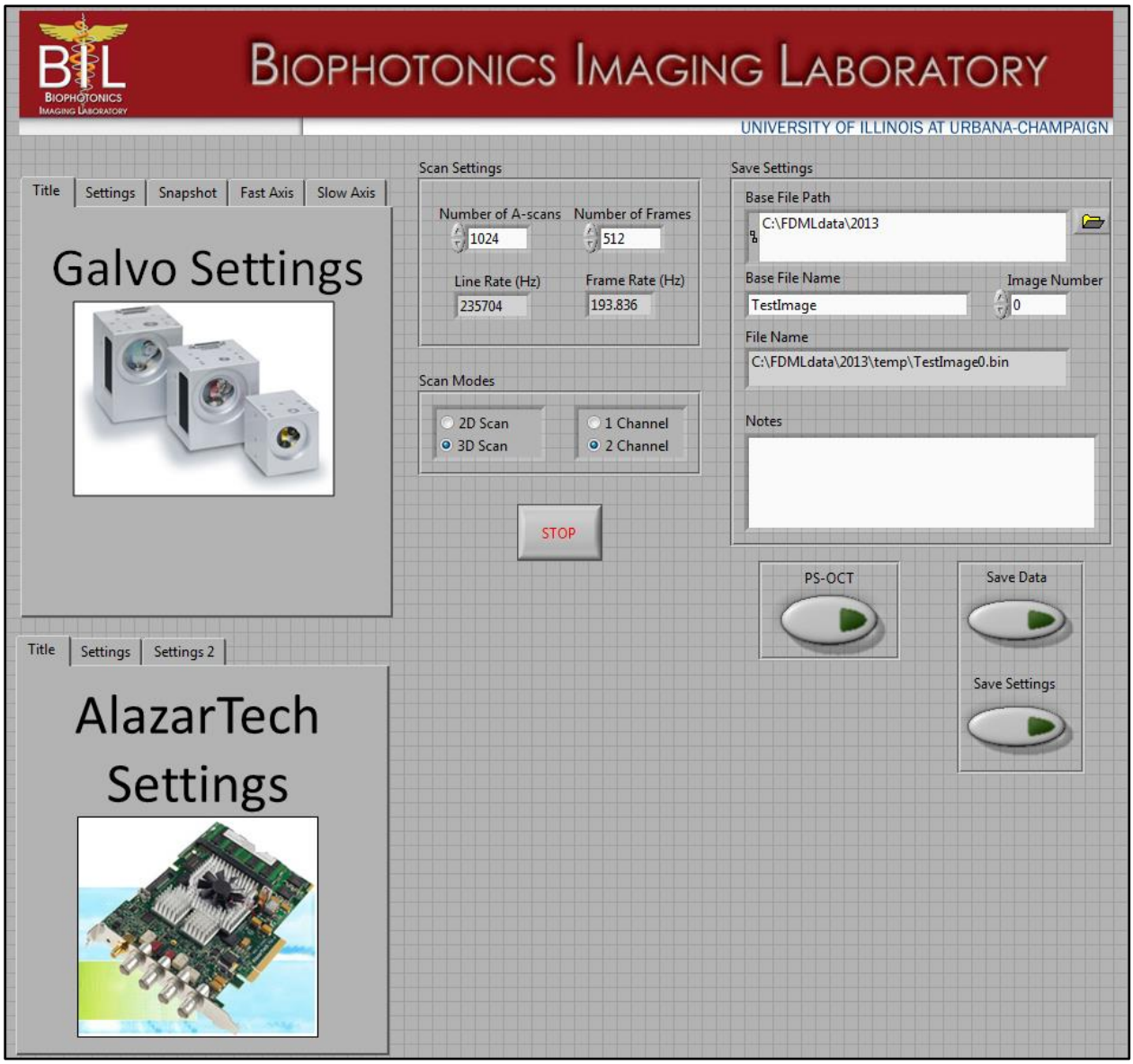

Figure 4.8 LabVIEW interface for user control of the swept-source PS-OCT system.

PS-OCT requires two A-lines for each location, doubling the amount of data in comparison with standard OCT. This places an additional burden on the acquisition and processing hardware. The swept-source interferometer developed in this thesis acquires two channels of 12 bit data at 250 MS/s each, for a total acquisition rate of 1 GB/s. The ATS9350 DAQ card has 128 MB of high-speed onboard RAM that serves as a buffer to prevent data overflow during transfer to the

PC. Data transfer over the PCIe x8 bus is approximately 1.6 GB/s. The ATS9350 provides direct memory access (DMA) for data transfer to the PC memory. This allows for the data to be transferred asynchronously with respect to the data acquisition. During the PS-OCT acquisition a frame of A-scans are combined and transferred as a single buffer. The DMA process is illustrated in Figure 4.9.

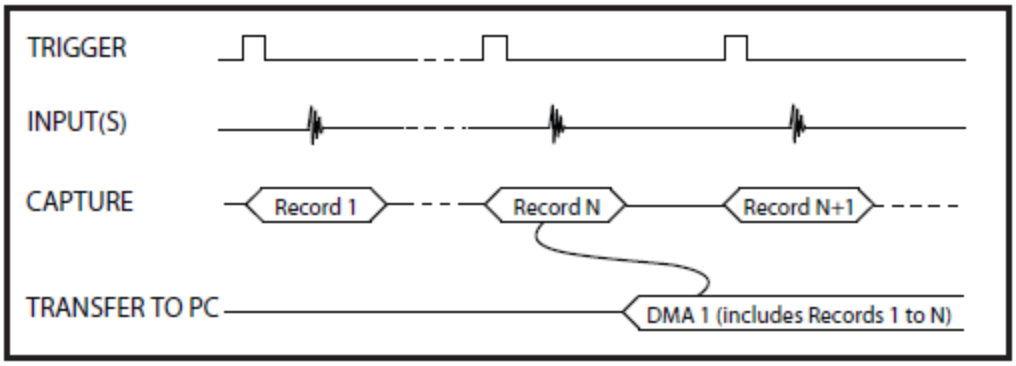

Figure 4.9 Illustration of ATS9350 data acquisition and transfer. A record corresponds to a single A-scan. DMA: direct memory access [77].

The acquisition and processing dataflow is illustrated in Figure 4.10. Each frame is digitized by the ATS9350 and transferred using DMA to the CPU RAM. The data is stored in page-locked, or pinned, memory. This prevents the CPU from swapping this memory space to the hard disk, ensuring that it is always available for immediate access by the GPU. The raw data is transferred frame-by-frame to the GPU where it is processed. Either the structural OCT or phase retardation data is displayed depending on the user selection in the LabVIEW interface. Following acquisition of the entire volume, the raw data is saved to disk.

The GPU used in this thesis is the NVIDIA GeForce GTX 285 which has 1 GB of onboard RAM and 240 cores. Processing is performed using the CUDA Toolkit 4.1. GPUs specialize in processing a multitude of threads simultaneously. The CUDA programming model is designed to allow the GPU parallel processing capabilities to be used for general purpose processing. Threads are organized into a grid of thread blocks, where each thread block is required to operate independently of the others. This organization is illustrated in Figure 4.11. The maximum threads per block on the GTX 285 is 512. Block dimensions of 32 x 16 are used.

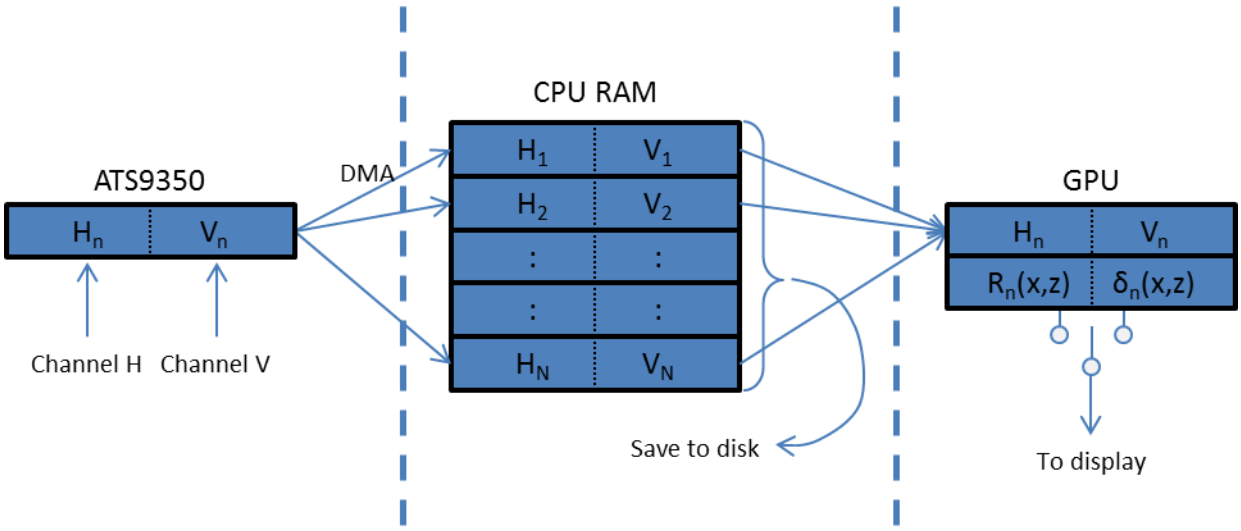

Figure 4.10 Dataflow for PS-OCT acquisition and processing. DMA: direct memory access.

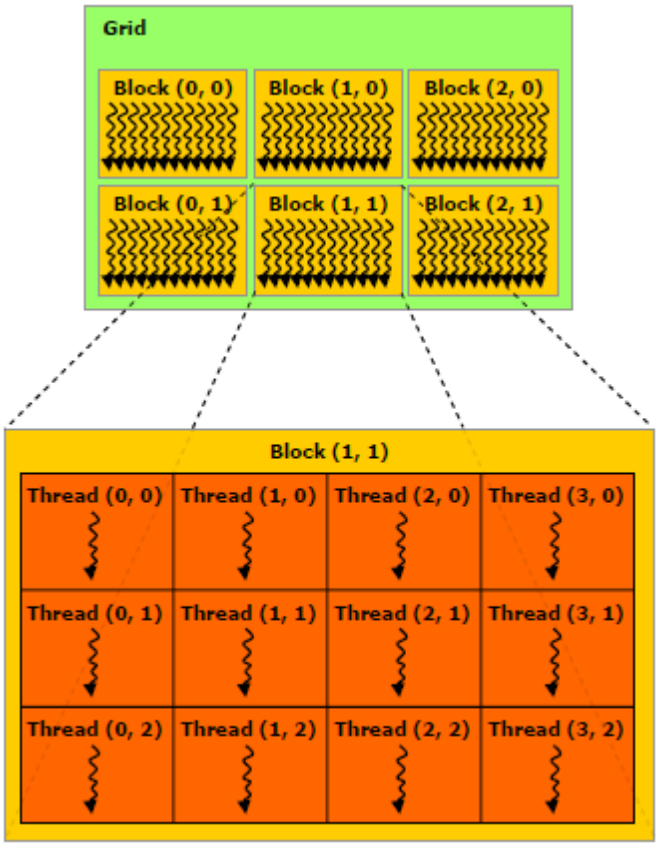

Figure 4.11 Illustration of the CUDA thread organization [78].

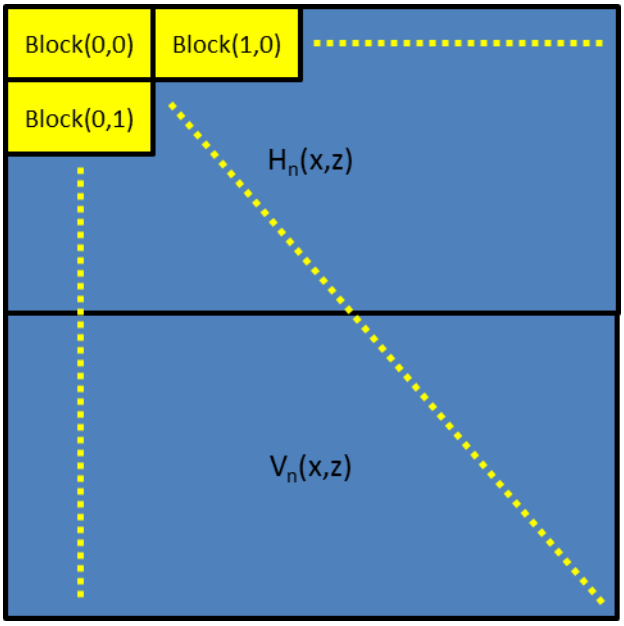

Figure 4.12 Thread organization for parallel processing of the horizontal and vertical polarization measurements.

The code is written in kernels which are executed by each thread. The block index and thread index determine which pixel the specific thread processes. For processing both the horizontal and vertical polarization channels simultaneously, the blocks are organized as shown in Figure 4.12. When calculating the values of R and δ, a single thread operates upon the appropriate pixels in both H and V.

The processing steps performed on the GPU are listed in Figure 4.13. Processing on the GPU is performed in the single-precision floating-point data format. This requires conversion of the raw data from the unsigned 16-bit integer and subtraction of the DC offset introduced by the unsigned data. Resampling is performed using linear interpolation followed by multiplication with a Tukey window to reduce side lobes. The resampling indices and the windowing function are generated in MATLAB and loaded into the GPU memory prior to the acquisition. A real-to-complex Fast-Fourier-Transform (FFT) is performed using the cuFFT library. The DC pixel is removed from the result. The desired OCT or PS-OCT signal is then calculated. The value of R is gamma compressed with a gamma value of 0.5. Lastly, the data is rescaled and converted to unsigned 16-bit integer format for display purposes.

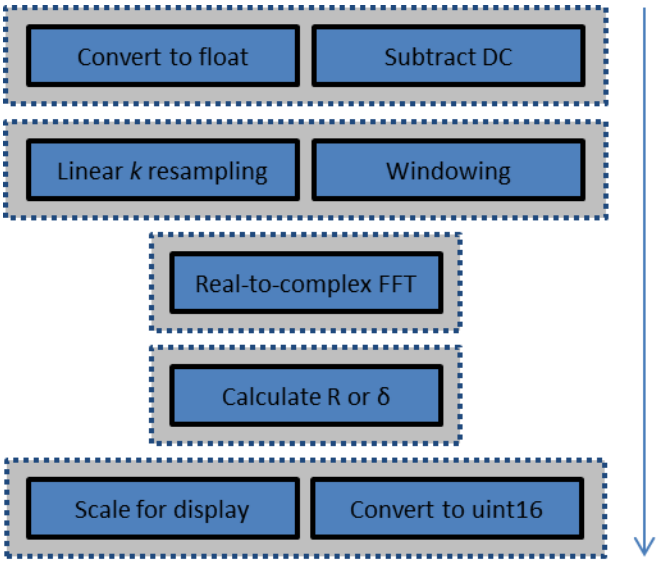

Figure 4.13 Processing steps. Each row represents a single kernel.

Display of the data is performed using OpenGL 3.3. This allows the data to be displayed directly from the GPU, making data transfer back to the CPU RAM unnecessary. The pixel data is stored in a 2D texture object called a pixel buffer object. This object is used to perform pixel-based operations. Ownership of this object can be transferred between OpenGL and CUDA to allow the kernel to update the pixel data. This update occurs in the final kernel. The process is illustrated in Figure 4.14.

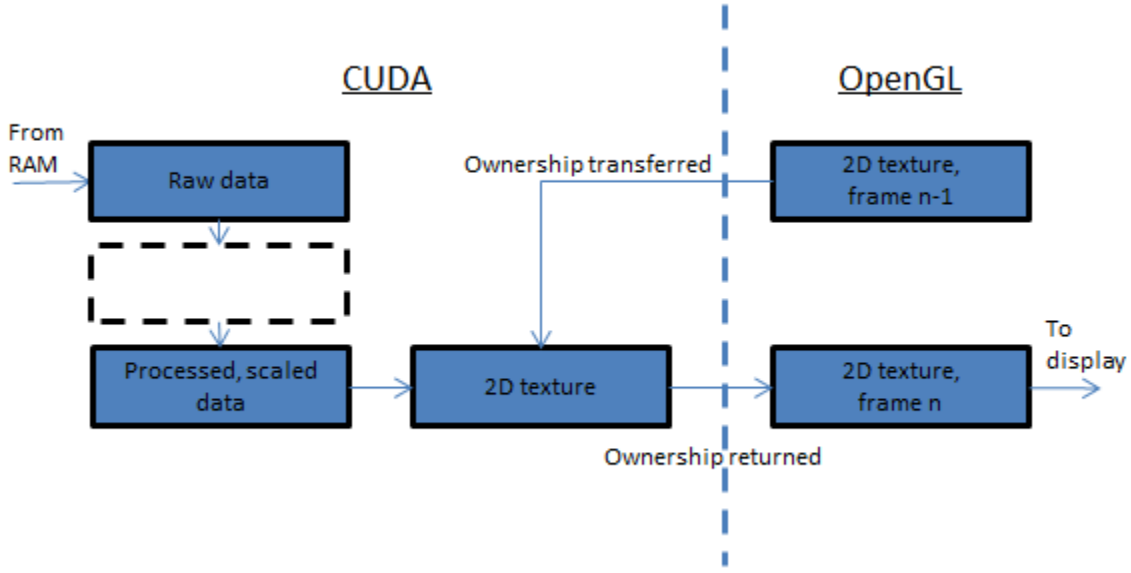

Figure 4.14 Interoperability between CUDA and OpenGL by transferring ownership of the 2D texture.

Creation of the OpenGL context and display window is done using the GLFW library. OpenGL geometry operations are performed using the GLM library. The frame is situated along the *x*-*y* axis with the view port on the positive *z*-axis looking toward the origin. An orthographic projection is used to remove parallax. For speed and compatibility purposes, the red-green-blue-alpha (RGBA) pixel type is used. The alpha value is set to be opaque and the RGB values are set equal to give the desired grayscale image.

Previously published PS-OCT processing speeds recorded possible processing speeds of 80,000 lines per second using parallel CPU processing on three 2.66 GHz cores [79]. However, the real-time implementation was limited by the transfer speed of the digitizer to 20,000 lines per second. For additional comparison, parallel processing was implemented using MATLAB. Non-optimized parallel processing on twelve 2.60 GHz cores achieved approximately 55,000 lines per second. Due to the combination of the high-speed laser, acquisition hardware, and GPU processing, the system in this thesis far exceeds these rates. GPU processing time, including reading from the CPU RAM and updating the display, is approximately 185,000 lines per second. This is an order of magnitude improvement over the previously published CPU speed.

Screenshots of the real-time display for both OCT and PS-OCT processing are shown in Figure 4.15. The typical settings used for imaging are 960 samples per A-scan, corresponding to 480 depth pixels, and 1024 A-scans per frame. The field-of-view is approximately 3.45 mm in both the transverse and axial dimensions. The sample is molded plastic which exhibits stress birefringence. While the structural OCT data appears homogeneous, the phase retardation information highlights the internal stress on the plastic.

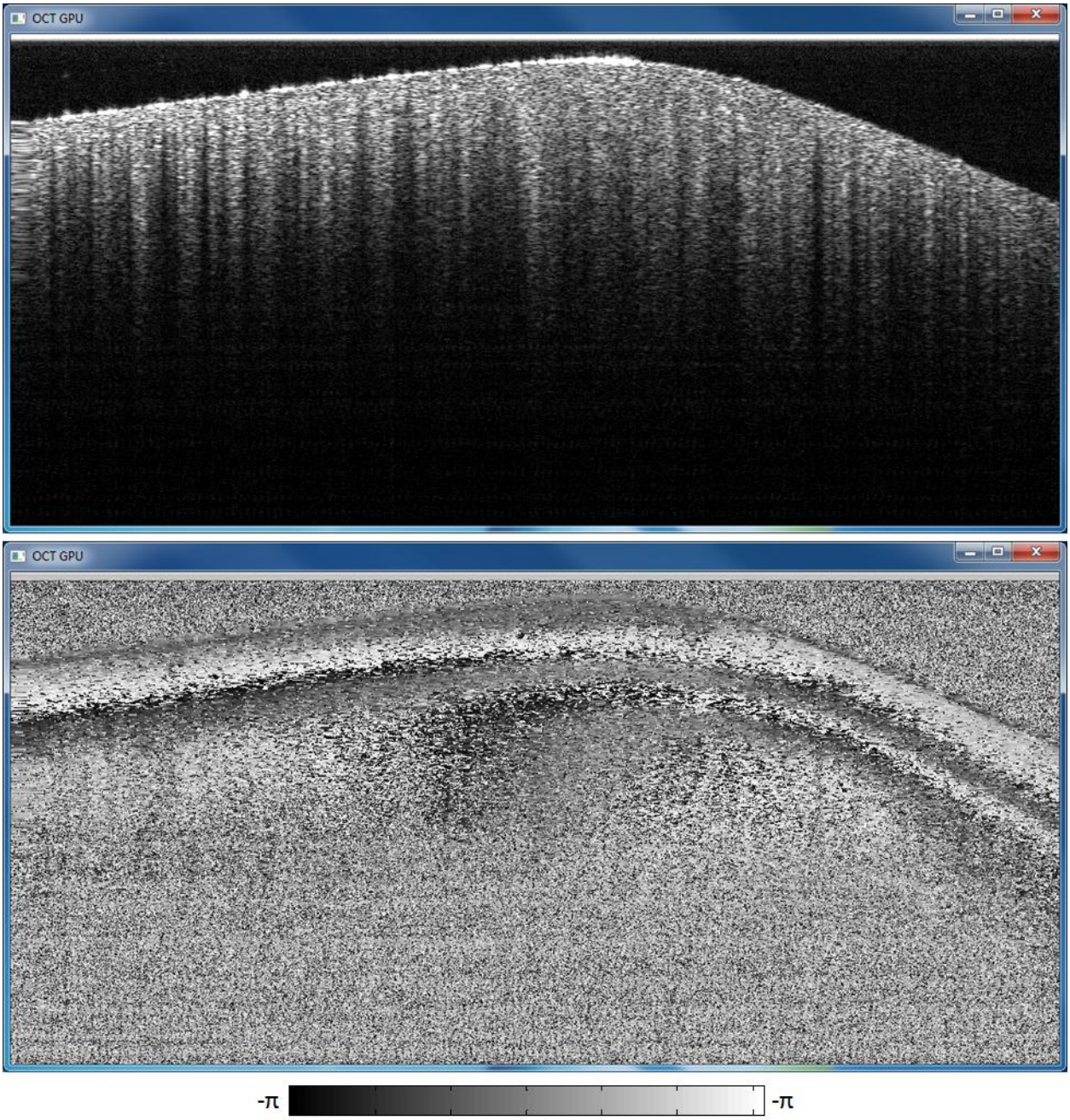

Figure 4.15 Two screenshots of the real-time display while imaging a molded plastic sample. The sample exhibits significant birefringence. Top: OCT structural image. Bottom: PS-OCT phase retardation image. A color scale has been included for reference.

5 PS-OCT Imaging of the Human Breast

5.1 Imaging study

An *ex vivo* imaging study was performed to explore the biological features of the human breast using PS-OCT. Fresh human tissue was acquired through a protocol approved by the institutional review boards of both the University of Illinois at Urbana-Champaign and Carle Foundation Hospital. Samples of excess mastectomy tissue not used for clinical diagnosis were provided for imaging at the University of Illinois at Urbana-Champaign. The tissue was transported in cold saline solution, and imaging was performed within 12 hours of excision.

Tissue was obtained from a total of six female patients, ages 32 through 68, with an average age of 49 years. Each tissue sample was labeled as "normal" or "diseased" based on the preliminary diagnosis of the pathology lab. Normal samples were received from all six patients, while diseased samples were received from four patients. The tissue samples were removed from saline and placed into a Petri dish for imaging. Occasionally the samples were bisected to provide access to suspicious areas. The samples were fixed and preserved in 10% formalin solution immediately after imaging. Following fixation the samples were embedded in paraffin and sectioned for staining. Slides stained with hematoxylin and eosin (H&E) were diagnosed by a board certified pathologist for comparison with the PS-OCT imaging results.

Tissue sections were also stained for collagen content using picrosirius red [80]. When imaged through cross-polarizers the birefringent collagen fibers appear in brilliant color. The color of the collagen varies from green to red and is determined by both the thickness and the packing of the fibers [81]. Thinner, less aligned fibers appear green. Thicker, more aligned fibers appear red.

The PS-OCT datasets were post-processed to provide an absolute measurement of the phase retardation. This is possible due to the careful calibration described in Section 4.2. The polarization state incident on the surface is known to be circular. Using an active contour surface detection algorithm the phase retardation was normalized to the known surface value. Pixels with

low OCT intensity were set to black to remove background noise and a high-contrast color map was used to display the phase retardation data. Both the OCT and PS-OCT datasets were interpolated to provide isometric pixel dimensions for improved comparison with histology.

Quantitative birefringence values were calculated for each tissue type. The birefringence value Δn was calculated using Equation (4.5).

$$\Delta n = \frac{\lambda_0}{4\pi} slope_{retardation} \tag{4.5}$$

The phase retardation slope was calculated using least squares regression. To reduce the effects of noise upon the calculation, a 50 μm median filter was applied along depth. A mean phase retardation profile was then calculated using an 80 μm wide sliding window. Some linear fits were not successful due to the heterogeneity of birefringence along depth. A fit was considered successful if the resulting R^2 value exceeded 0.5.

5.2 Normal breast tissues

The human breast consists of numerous glands known as lobules which are connected to the nipple via a network of ducts [82]. The interlobular tissue is composed of dense, fibrous stroma tissue. The entire lobule and duct system is suspended in adipose tissue which makes up the majority of the breast. A network of collagenous septa extends throughout the adipose tissue that separates the lobule units. An illustration of the breast structure is shown in Figure 5.1.

In structural OCT imaging the adipocytes are easily recognizable by their large size and their "empty" appearance due to their low scattering lipid interior, while the stroma appears moderately scattering. Adipocytes are clearly seen throughout the tissue in Figure 5.2. However, the vein-like fibrous tissue may be difficult to distinguish from a spiculated tumor invasion using only the structural image. Thankfully, the form birefringence of the collagen content makes the fibrous septa discernible. Figure 5.3 shows the corresponding PS-OCT phase retardation image. A color change along increasing depth corresponds to a change in polarization state due to the tissue birefringence. It can be seen that adipose does not affect the polarization state, while the

birefringent collagen tissue induces significant phase retardation. The stroma is also recognizable using the picrosirius red stain. This corresponds with the birefringence detected by the PS-OCT system.

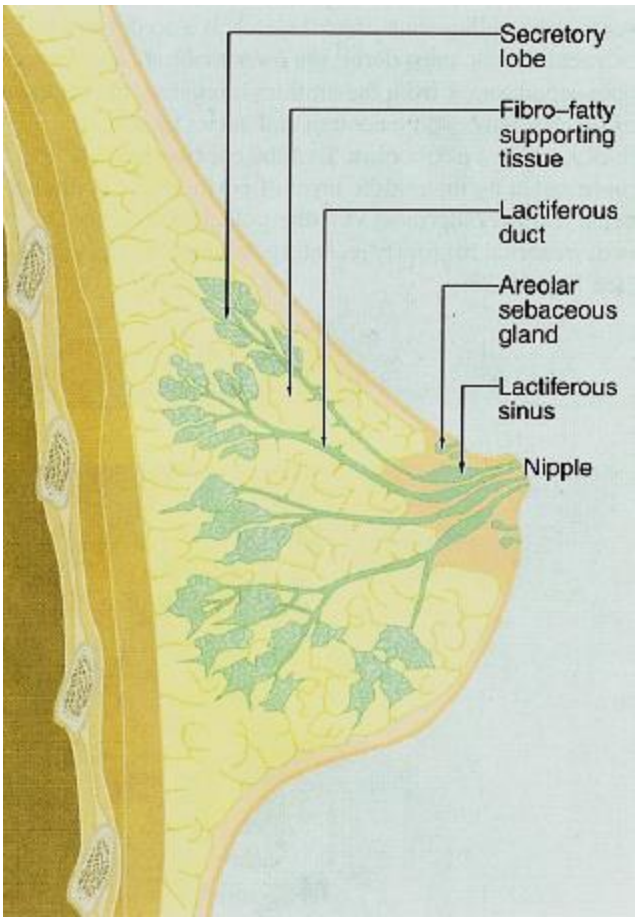

Figure 5.1 Illustration of human breast anatomy. The lobule-duct system is suspended in a mixture of adipose and collagen tissue [82].

The interlobular tissue is composed mainly of dense collagen fibers. This tissue appears homogeneously scattering in the structural OCT image as in Figure 5.4. It is difficult to determine the tissue microstructure from the homogenous OCT speckle alone. The PS-OCT results are shown in Figure 5.5. When stained with picrosirius red, the collagen fibers appear incredibly dense and bright. The fiber colors are concentrated in the long wavelength range implying that the fibers are also thick, tightly packed, and highly organized. This corresponds to a drastic change in phase retardation as seen in the PS-OCT image. While ducts can be clearly

seen in the histology, they are not apparent in the OCT image. The ducts may have been closed during imaging. In this case they would only be four cells thick and near the resolution limit of the system, making them difficult to distinguish from the highly scattering background.

The quantitative birefringence of stroma can be calculated over the two regions indicated by the left and right arrows in Figure 5.3 and the entire imaging area in Figure 5.5. Computation of the birefringence using a sliding window provides 620 suitable data points, resulting in a mean birefringence of 5.5×10^{-4} with a 95% confidence interval (CI) of $\pm3.7\times10^{-5}$ for normal stroma.

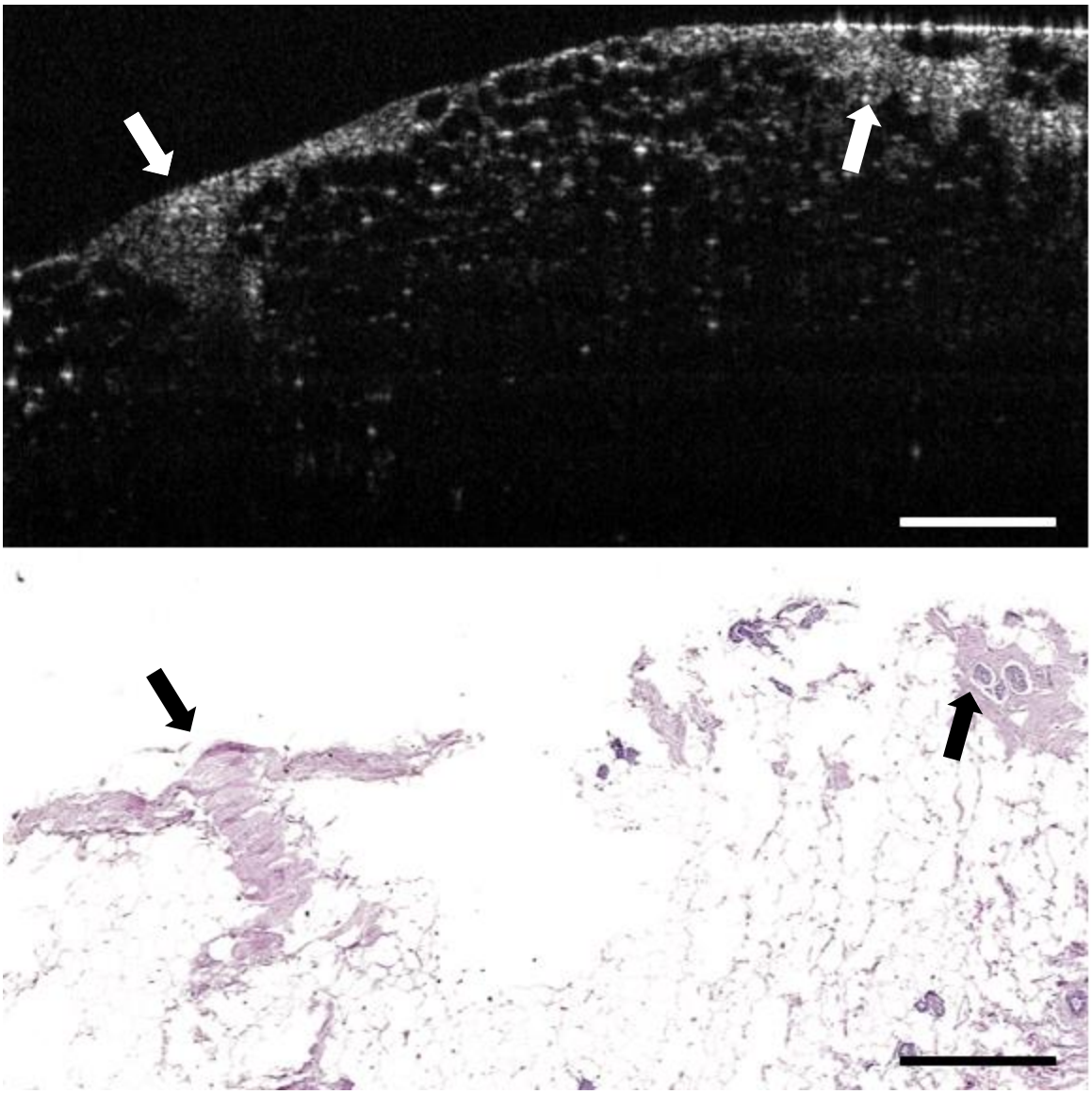

Figure 5.2 Top: Structural OCT image of typical breast tissue. Both adipose and stroma tissue are visible. The adipocytes appear as hollow shells, while the stroma (arrows) is moderately scattering. Bottom: Corresponding H&E histology section. Scale bars correspond to 500 µm.

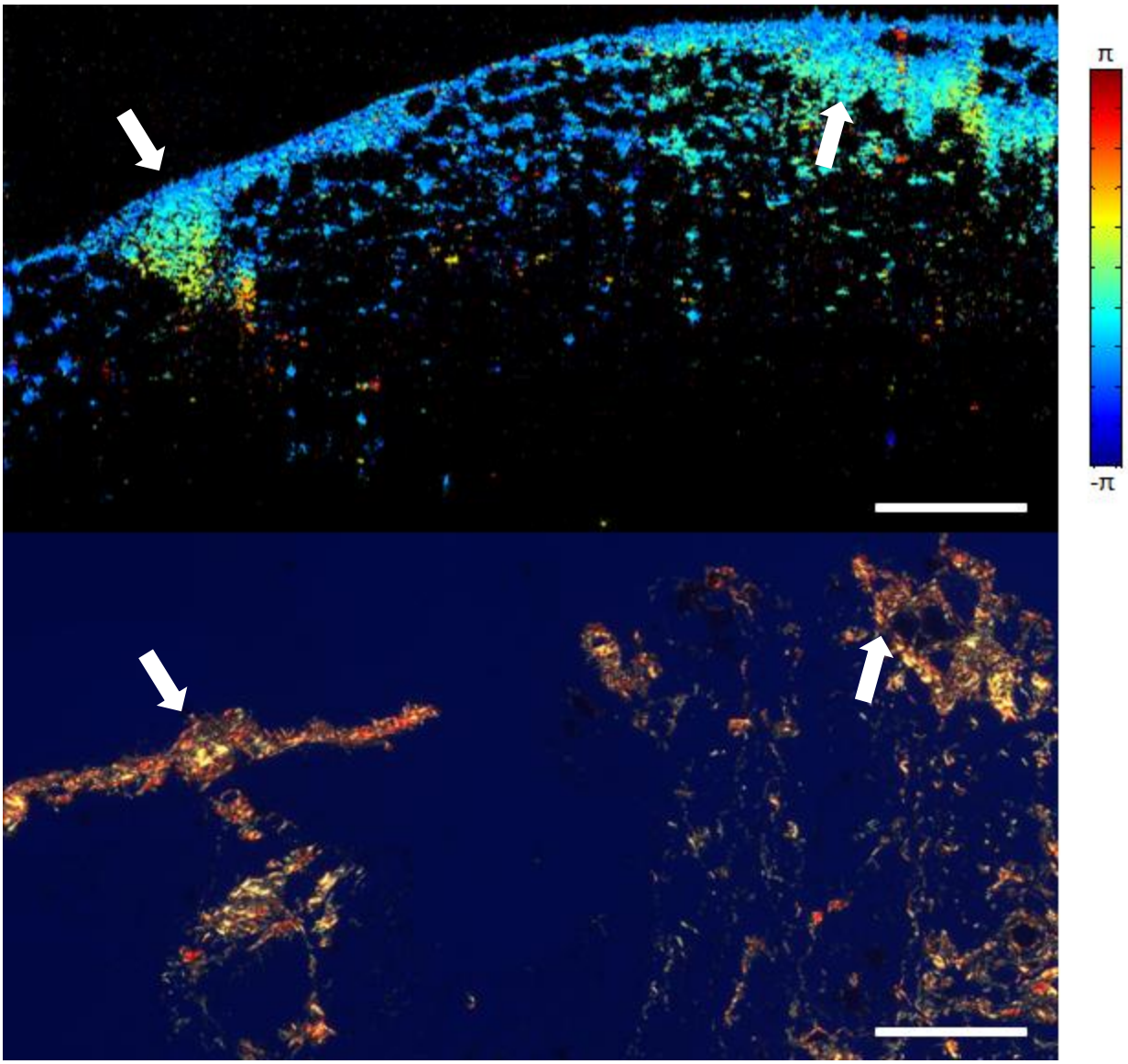

Figure 5.3 Top: PS-OCT phase retardation image of typical breast tissue. The adipocytes do not affect the polarization state. However, the fibrous stroma (arrows) generates significant phase retardation. Bottom: Corresponding picrosirius red histology section. Scale bars correspond to 500 µm.

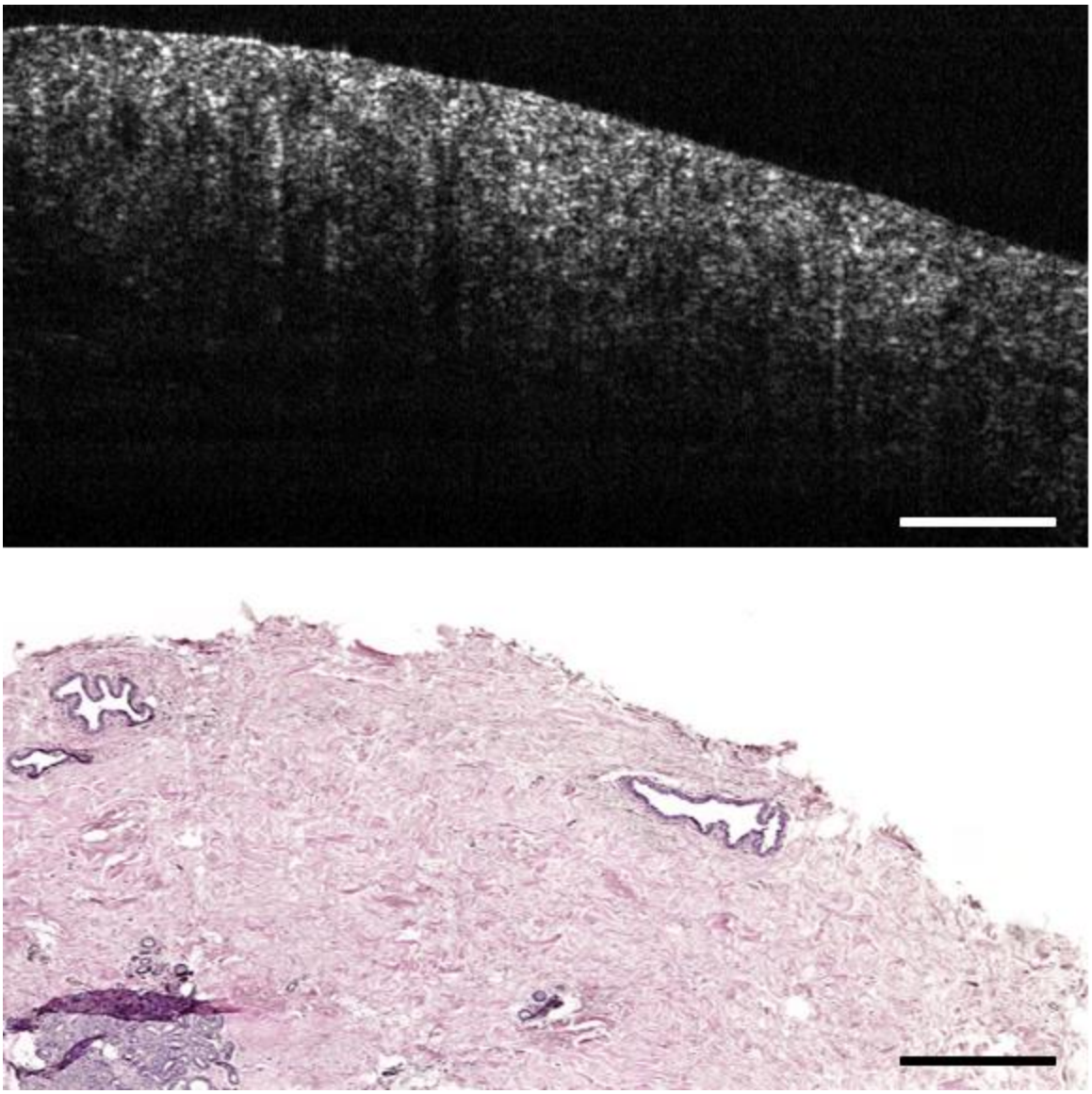

Figure 5.4 Top: Structural OCT image of fibrous breast tissue. The dense stroma appears as a homogeneous speckle pattern. Bottom: Representative H&E histology section. Scale bars correspond to 500 µm.

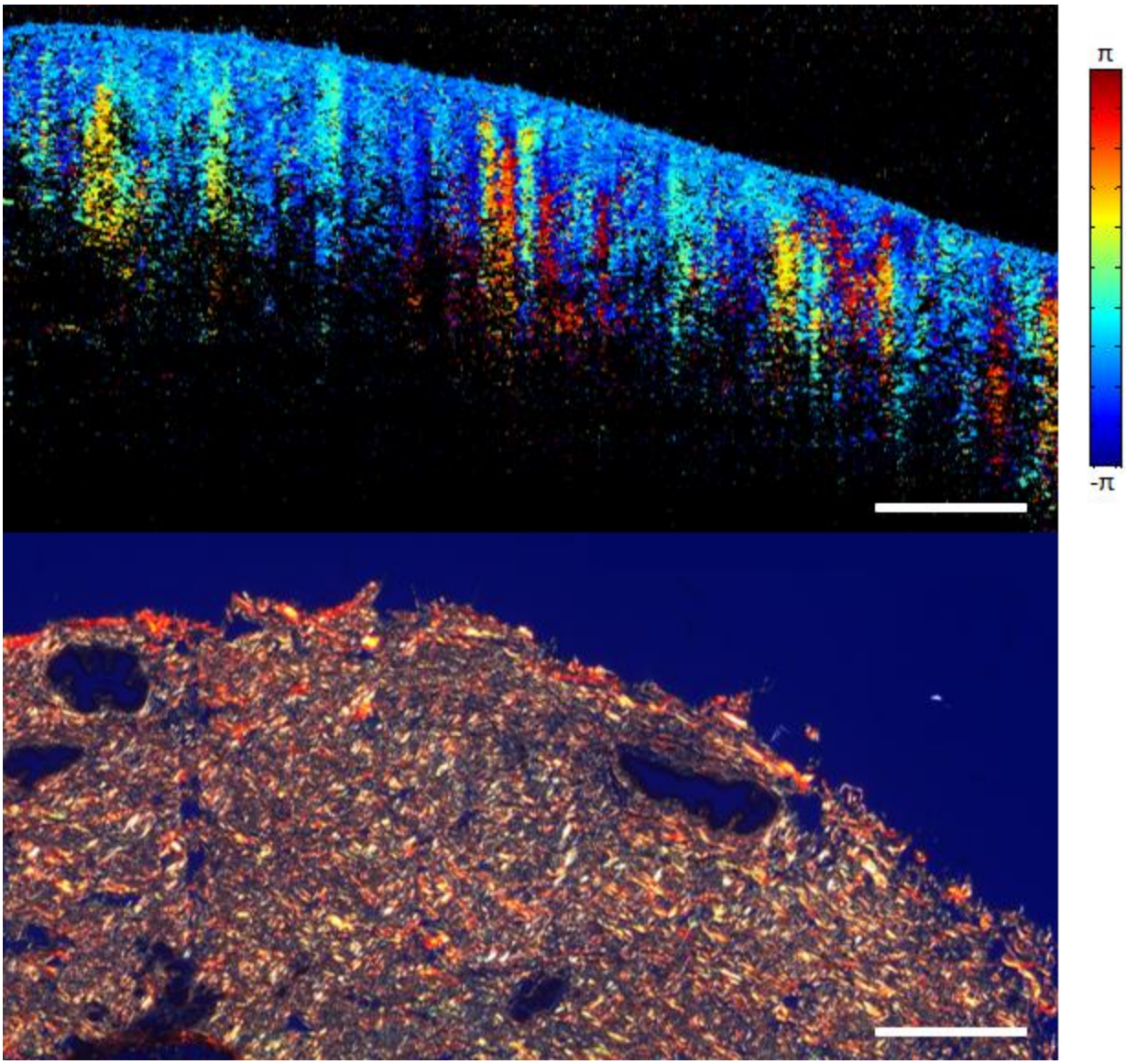

Figure 5.5 Top: PS-OCT phase-retardation image of fibrous breast tissue. The dense stroma greatly affects the polarization state. Bottom: Representative picrosirius red histology section. Scale bars correspond to 500 µm.

5.3 Cancerous tissues

The most common origin of breast cancer is from the cells in the ducts. This form of cancer is known as ductal-carcinoma *in-situ* (DCIS) [2]. Although it is non-invasive, it has the potential to become invasive and life threatening. Because of this it is often surgically removed. An advanced case of DCIS is shown in Figure 5.6 and Figure 5.7. The ducts are grossly enlarged and clearly abnormal even to the naked eye. The duct walls show micropapillae and a Roman bridge appearance typical of cribriform type DCIS [83]. Reflections from the secretions inside the ducts appear as a light speckle pattern on the structural OCT. The high phase retardation measurement suggests that the collagenous interlobular tissue is not affected by the presence of DCIS. This is confirmed by the picrosirius red staining which shows collagen content comparable to that seen in the normal fibrous stroma. This result is expected, as the cancer is presently limited to the interior of the ducts.

DCIS can progress and become invasive, breaking through the duct wall and infiltrating the surrounding tissue. This cancer form is known as invasive ductal carcinoma (IDC). It is capable of metastasizing to other areas of the body and is often deadly, making successful surgical removal imperative. The structural OCT image in Figure 5.8 appears incredibly similar to the OCT signature from fibrous stroma. This similarity severely complicates accurate prediction of the tumor margin status. It is clear from the picrosirius red stain that the invasive cancer has destroyed the organized collagen structure of the stroma. The color has also shifted toward shorter wavelengths indicating a change in collagen thickness and alignment. The effect of the collagen loss on phase retardation can be seen in Figure 5.9. The invasive tumor does not exhibit significant birefringence and therefore the phase retardation measurement is homogenous. Small pockets of collagen may remain, leading to a localized birefringence effect. However, the typical phase retardation signature is drastically different from that of normal stroma.

Quantitative measurement of both disease types confirms the qualitative differences described above. The region indicated by the arrow in Figure 5.7 can be used to calculate the

birefringence of stroma surrounding DCIS. The mean birefringence is $5.4\times10^{-4}\pm5.2\times10^{-5}$ (95% CI), nearly identical to the birefringence of healthy stroma (p-value = 0.82).

However, the birefringence of IDC is greatly decreased. The left half of the IDC imaging area indicated by the left arrow in Figure 5.9 has an average birefringence of $1.5\times10^{-4}\pm6.1\times10^{-5}$ (95% CI). The destruction of collagen content causes a significant drop in birefringence that is visible in the PS-OCT measurement ($p < 0.001$). The region indicated by the right arrow in Figure 5.9 has an average birefringence of $3.9\times10^{-4}\pm8.1\times10^{-5}$ (95% CI). While some collagen remains in this area, there is much less collagen than in the normal tissue. As a result, the calculated birefringence is also significantly lower ($p < 0.001$). A summary of the quantitative analysis is shown in Figure 5.10.

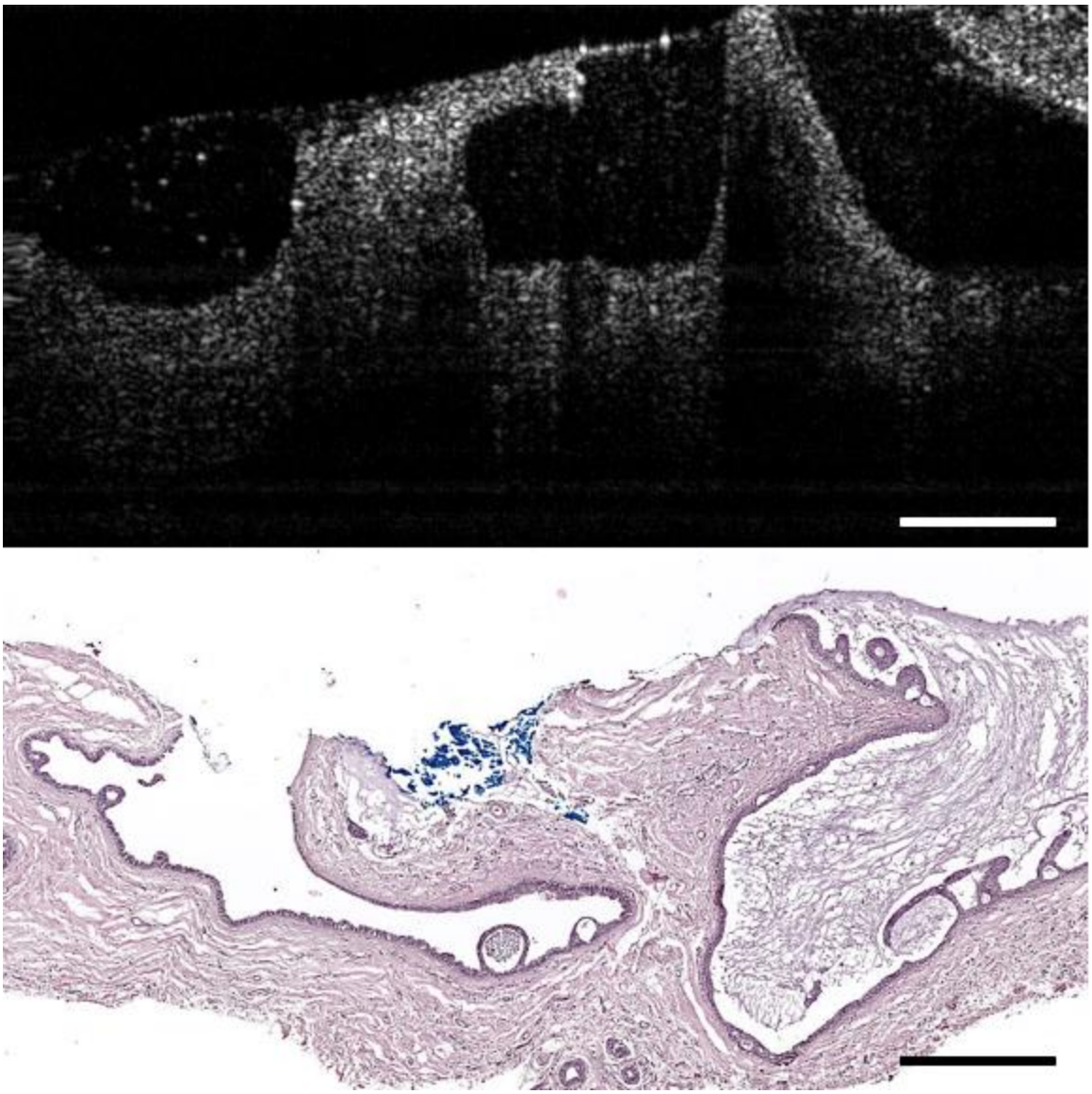

Figure 5.6 Top: Structural OCT image of ductal carcinoma *in-situ*. The ducts are grossly misshapen. Bottom: Representative H&E histology section. Scale bars correspond to 500 µm.

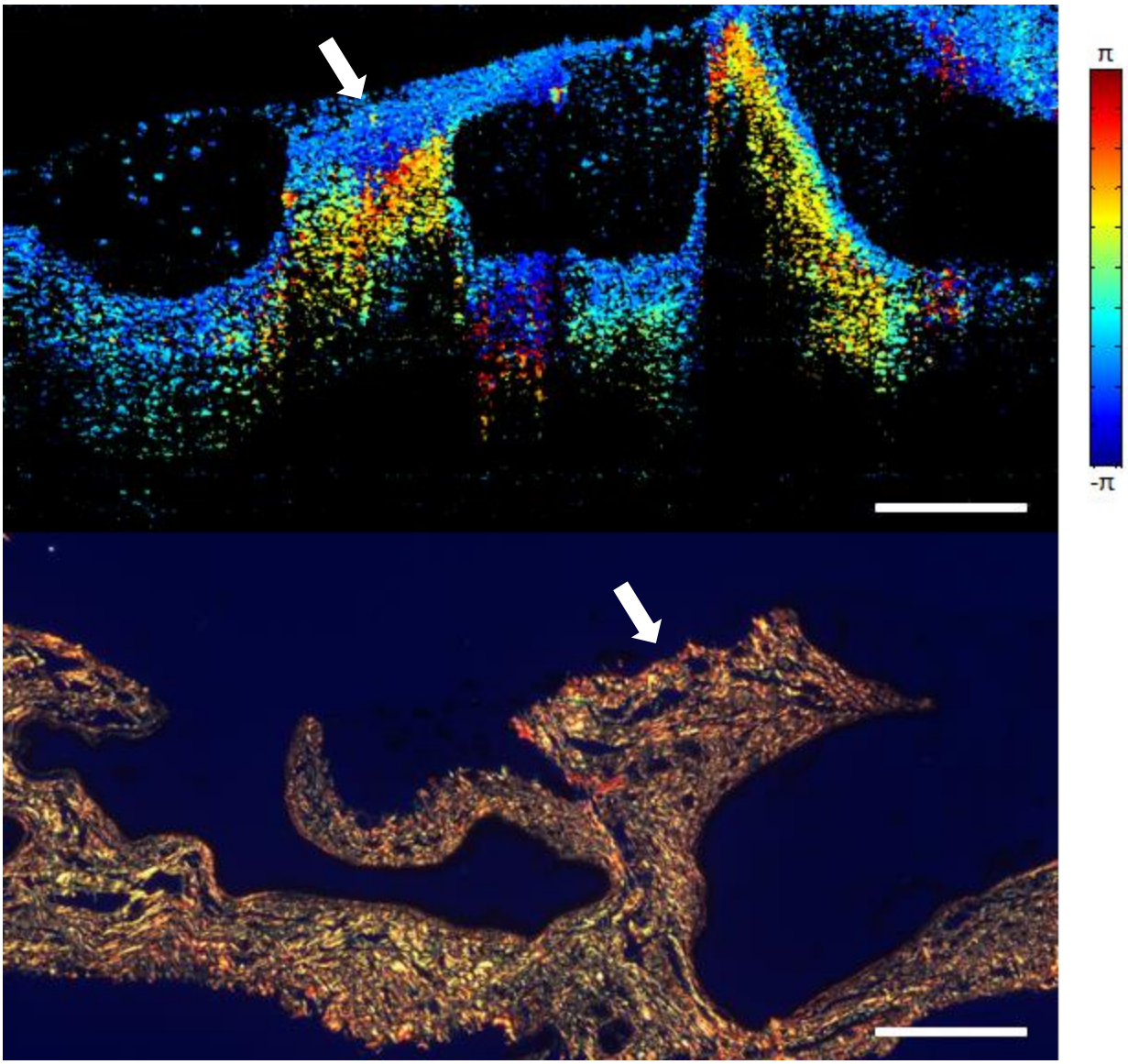

Figure 5.7 Top: PS-OCT phase retardation image of ductal carcinoma *in-situ*. The surrounding stroma (arrow) causes significant phase retardation as seen in Section 5.2. Bottom: Representative picrosirius red histology section. Scale bars correspond to 500 μm.

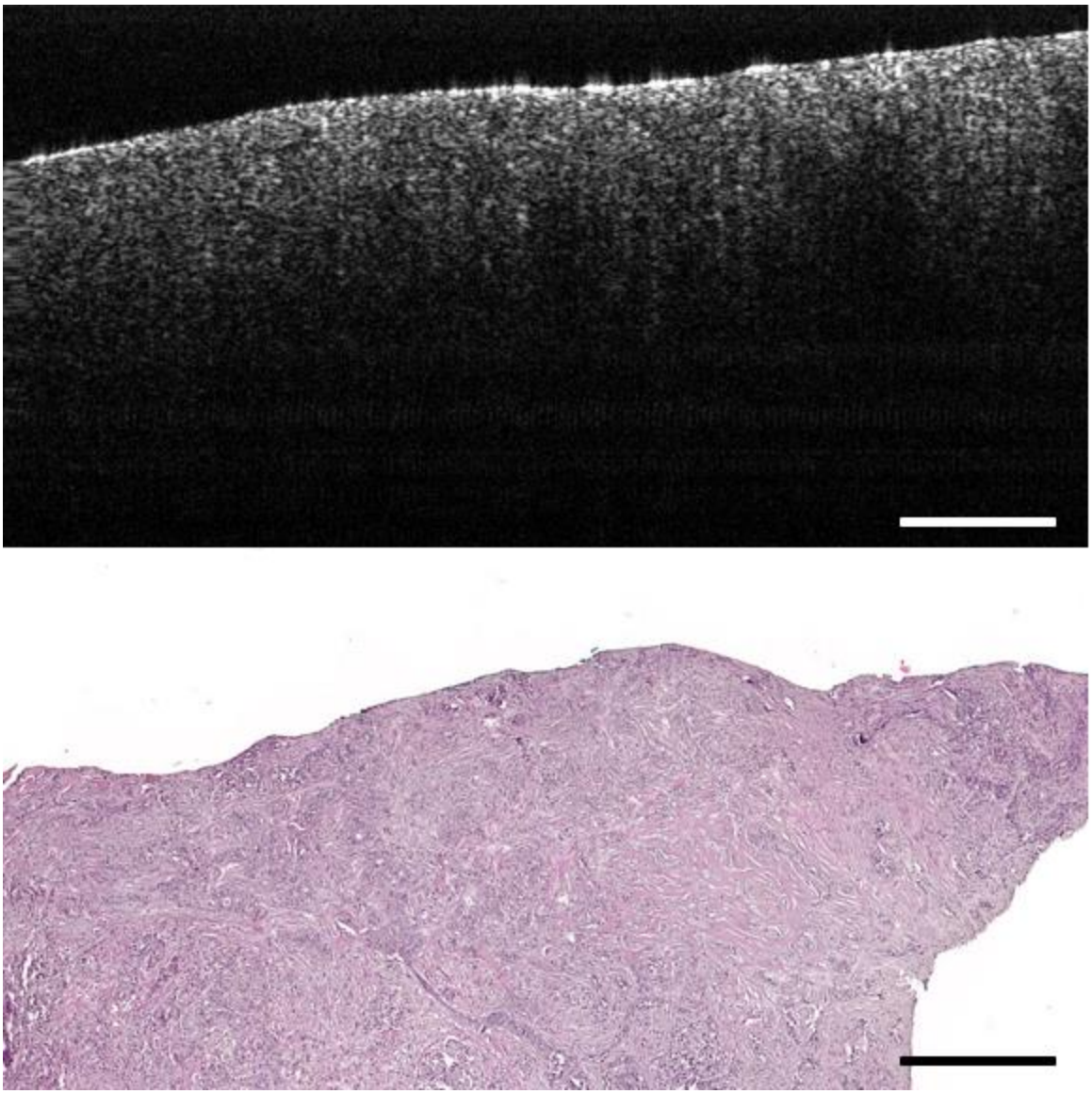

Figure 5.8 Top: Structural OCT image of invasive ductal carcinoma. The tissue appears homogenously scattering. Bottom: Representative H&E histology section. Scale bars correspond to 500 µm.

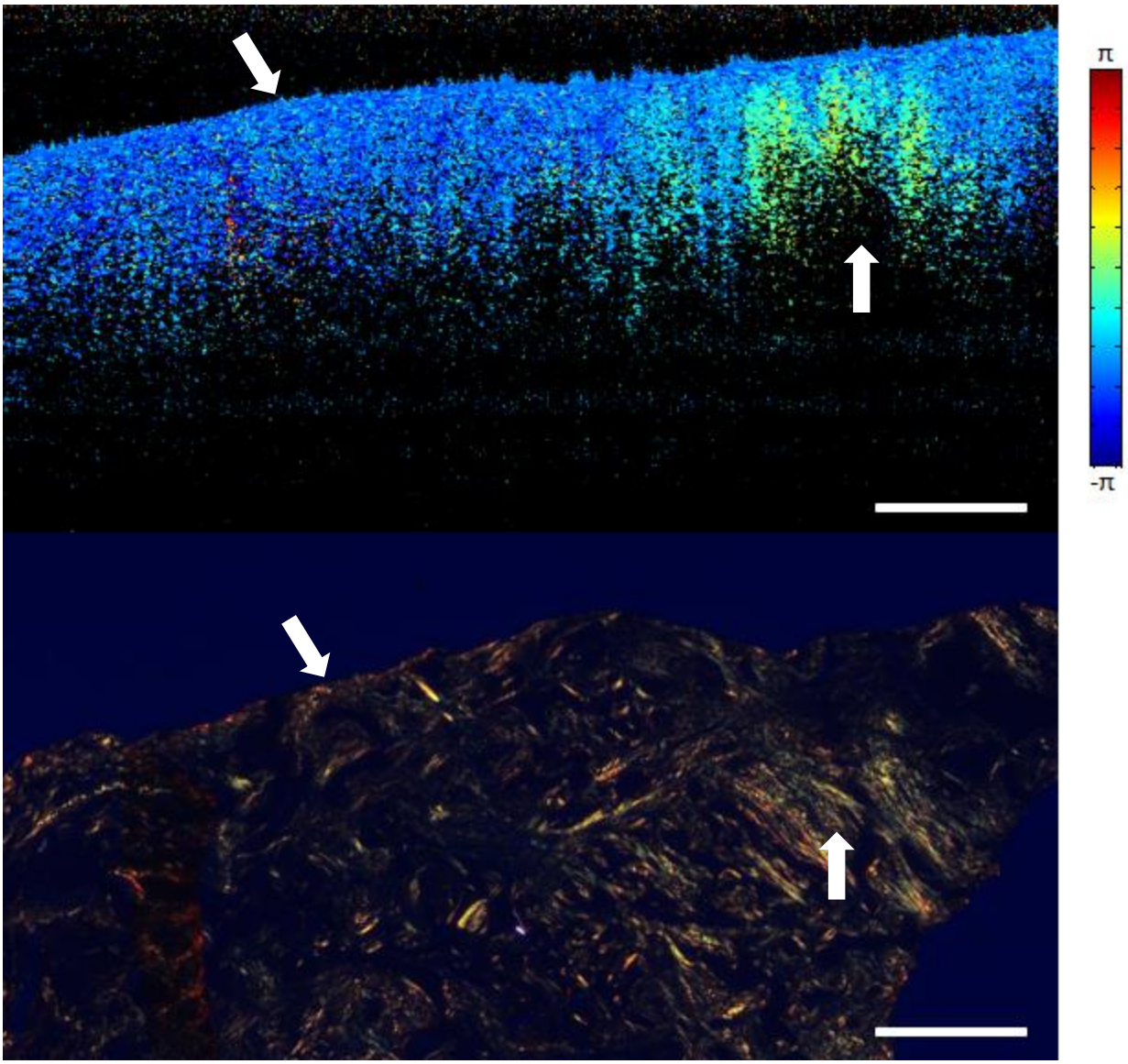

Figure 5.9 Top: PS-OCT phase retardation image of invasive ductal carcinoma. The organized collagen structure has been destroyed (left arrow) by the invading tumor, leading to a homogeneous polarization state. The small area of birefringence (right arrow) is suspected to correspond to a pocket of remaining collage. Bottom: Representative picrosirius red histology section. Scale bars correspond to 500 μm.

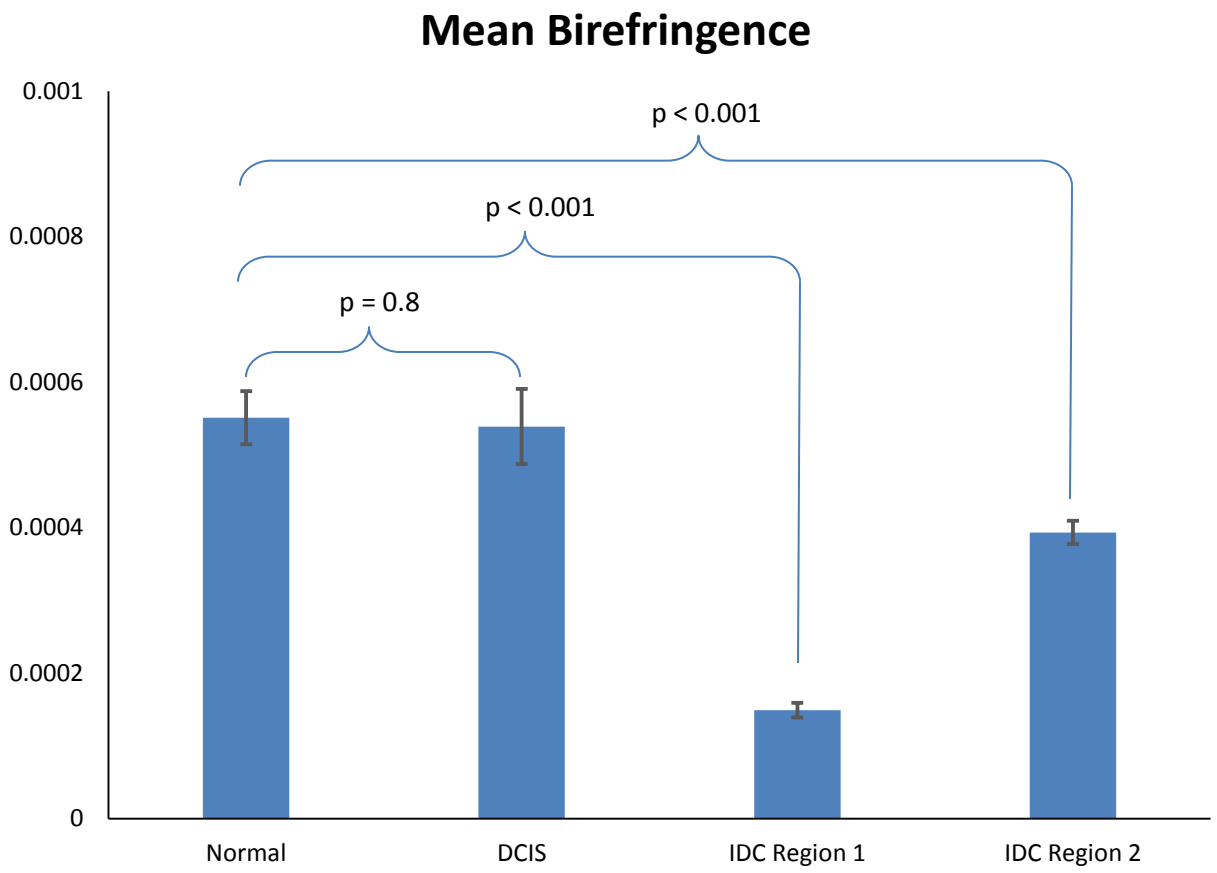

Figure 5.10 Quantitative birefringence measurement of normal and diseased tissue types. Error bars correspond to 95% confidence intervals. IDC Regions 1 and 2 correspond to the left and right arrows in Figure 5.9, respectively. The stroma surrounding DCIS is not significantly different than healthy stroma (p-value = 0.8). However, IDC shows a significant change in birefringence (p-value < 0.001). Data points: Normal n = 620, DCIS n = 76, IDC Region 1 n = 142, IDC Region 2 n = 103.

6 Conclusion

6.1 Summary

There is currently no widely available method for real-time intraoperative assessment of tumor margin status. While OCT has had much success in this area, it remains difficult to distinguish between dense normal and cancerous tissues using backscattered intensity alone. In Chapter 1 it was shown that PS-OCT has previously been used to detect changes in form birefringence due to collagen alignment in biological tissues. PS-OCT was proposed as a real-time imaging method to provide enhanced contrast for tumor margin evaluation.

Chapters 2 and 3 presented a mathematical model that was used to describe the PS-OCT imaging system. Chapter 4 detailed the real-time PS-OCT system developed for this thesis. The FDML swept-source laser was successfully implemented in a double-buffered setup, and a calibration arm was designed to allow its use in a high-speed OCT interferometer. The polarization-sensitive interferometer was designed using single-mode fiber with an initial calibration procedure. Real-time processing and display were implemented at record speeds utilizing high-speed data acquisition hardware and parallel processing on a GPU.

The imaging results in Chapter 5 successfully demonstrate enhanced contrast between normal and cancerous tissue. Both normal and cancerous breast tissues were investigated using real-time PS-OCT imaging. A post-processing algorithm was then used to recover the absolute phase retardation measurement for analyzing datasets taken over several different imaging sessions. The polarization information was found to provide significantly enhanced contrast between healthy tissue and invasive cancer in comparison with the traditional structural image. The stroma tissue was identifiable by its high birefringence both in the dense interlobular tissue and the fibrous septa. DCIS by nature does not appear to alter the birefringence properties of the surrounding tissue. However, it may still be possible to diagnose using structural OCT imaging [16, 18]. Lastly, IDC dramatically alters the collagen content leading to loss of birefringence.

This allows IDC to be distinguished from the fibrous stroma, suggesting the PS-OCT may provide the necessary contrast for determining tumor margin status.

6.2 Future work

For ideal intraoperative applications, the system must not be sensitive to movement of the fibers. A Jones matrix or polarization-maintaining fiber design should be explored to overcome this limitation to allow implementation in a hand-held probe. Additionally, while swept-source OCT is currently preferred for high-speed portable imaging, OCT spectrometers are becoming faster and decreasing in cost. Future generations of this system should consider the current state of the technology to choose the most appropriate option.

The results presented in Chapter 5 of this thesis encourage further exploration of PS-OCT imaging in breast cancer applications. Certain disease types remain to be explored. The benign fibroadenoma is of special interest as it may often be mistaken for invasive carcinoma. Previous reports have found fibroadenoma to be highly birefringent in comparison to IDC [26]. It is desirable to confirm these results with the picrosirius red staining and the real-time imaging system developed in this thesis. This thesis explored ductal carcinoma only. It will be important to understand the PS-OCT signature of lobular carcinoma as well.

A local, depth resolved birefringence measurement may be preferred for breast imaging due to the heterogeneity of the tissue along depth. A pixel-by-pixel measurement of the birefringence could reveal highly birefringent properties of tissue features that may be too small or complex to detect using the round-trip phase retardation. As an example, solid type DCIS may appear as an area of high scattering and low birefringence hidden within the highly birefringent stroma. Additionally, quantification of the results could provide expected birefringence values for each disease type. This could be used to increase confidence during intraoperative margin assessment.

References

[1] A. Jemal, F. Bray, M. M. Center, J. Ferlay, E. Ward, and D. Forman, "Global cancer statistics," *CA: A Cancer Journal for Clinicians,* vol. 61, pp. 69-90, Mar-Apr 2011.

[2] American Cancer Society, *Breast Cancer Facts & Figures 2011-2012*. Atlanta, GA: American Cancer Society, Inc., 2011.

[3] G. P. Swanson, K. Rynearson, and R. Symmonds, "Significance of margins of excision on breast cancer recurrence," *American Journal of Clinical Oncology-Cancer Clinical Trials,* vol. 25, pp. 438-441, Oct 2002.

[4] M. F. Dillon, A. D. K. Hill, C. M. Quinn, E. W. McDermott, and N. O'Higgins, "A pathologic assessment of adequate margin status in breast-conserving therapy," *Annals of Surgical Oncology,* vol. 13, pp. 333-339, Mar 2006.

[5] A. Luini, J. Rososchansky, G. Gatti, S. Zurrida, P. Caldarella, G. Viale, G. R. dos Santos, and A. Frasson, "The surgical margin status after breast-conserving surgery: Discussion of an open issue," *Breast Cancer Research and Treatment,* vol. 113, pp. 397-402, Jan 2009.

[6] J. K. Karwowski, R. B. Jeffrey, I. R. McDougall, and R. J. Weigel, "Intraoperative ultrasonography improves identification of recurrent thyroid cancer," *Surgery,* vol. 132, pp. 924-928, Dec 2002.

[7] V. E. Strong, J. Humm, P. Russo, A. Jungbluth, W. D. Wong, F. Daghighian, L. Old, Y. Fong, and S. M. Larson, "A novel method to localize antibody-targeted cancer deposits intraoperatively using handheld PET beta and gamma probes," *Surgical Endoscopy and Other Interventional Techniques,* vol. 22, pp. 386-391, Feb 2008.

[8] T. P. Olson, J. Harter, A. Munoz, D. M. Mahvi, and T. M. Breslin, "Frozen section analysis for intraoperative margin assessment during breast-conserving surgery results in low rates of re-excision and local recurrence," *Annals of Surgical Oncology,* vol. 14, pp. 2953-2960, Oct 2007.

[9] E. K. Valdes, S. K. Boolbol, J. M. Cohen, and S. M. Feldman, "Intra-operative touch preparation cytology; does it have a role in re-excision lumpectomy?," *Annals of Surgical Oncology,* vol. 14, pp. 1045-1050, Mar 2007.

[10] S. Goldfeder, D. Davis, and J. Cullinan, "Breast specimen radiography: Can it predict margin status of excised breast carcinoma?," *Academic Radiology,* vol. 13, pp. 1453-1459, Dec 2006.

[11] B. Erguvan-Dogan, G. J. Whitman, V. A. Nguyen, M. J. Dryden, R. J. Stafford, J. Hazle, K. R. McAlee, M. J. Phelps, M. F. Ice, H. M. Kuerer, and L. P. Middleton, "Specimen radiography in confirmation of MRI-guided needle localization and surgical excision of breast lesions," *American Journal of Roentgenology,* vol. 187, pp. 339-344, Aug 2006.

[12] F. A. South, M. Marjanovic, and S. A. Boppart, "Intraoperative optical coherence tomography for cancer surgery," in *Optical Coherence Tomography: Technology and Applications*, W. Drexler and J. G. Fujimoto, Eds., 2nd ed, in press.

[13] D. Huang, E. A. Swanson, C. P. Lin, J. S. Schuman, W. G. Stinson, W. Chang, M. R. Hee, T. Flotte, K. Gregory, C. A. Puliafito, and et al., "Optical coherence tomography," *Science*, vol. 254, pp. 1178-81, Nov 1991.

[14] S. A. Boppart, W. Luo, D. L. Marks, and K. W. Singletary, "Optical coherence tomography: Feasibility for basic research and image-guided surgery of breast cancer," *Breast Cancer Research and Treatment*, vol. 84, pp. 85-97, Mar 2004.

[15] B. J. Vakoc, D. Fukumura, R. K. Jain, and B. E. Bouma, "Cancer imaging by optical coherence tomography: Preclinical progress and clinical potential," *Nature Reviews Cancer*, vol. 12, pp. 363-368, May 2012.

[16] P. L. Hsiung, D. R. Phatak, Y. Chen, A. D. Aguirre, J. G. Fujimoto, and J. L. Connolly, "Benign and malignant lesion in the human breast depicted with ultrahigh resolution and dimensional optical coherence tomography," *Radiology*, vol. 244, pp. 865-874, Sep 2007.

[17] F. T. Nguyen, A. M. Zysk, E. J. Chaney, J. G. Kotynek, U. J. Oliphant, F. J. Bellafiore, K. M. Rowland, P. A. Johnson, and S. A. Boppart, "Intraoperative evaluation of breast tumor margins with optical coherence tomography," *Cancer Research*, vol. 69, pp. 8790-8796, Nov 2009.

[18] C. Zhou, D. W. Cohen, Y. H. Wang, H. C. Lee, A. E. Mondelblatt, T. H. Tsai, A. D. Aguirre, J. G. Fujimoto, and J. L. Connolly, "Integrated optical coherence tomography and microscopy for ex vivo multiscale evaluation of human breast tissues," *Cancer Research*, vol. 70, pp. 10071-10079, Dec 2010.

[19] F. South, M. Marjanovic, S. G. Adie, E. J. Chaney, P. Ray, K. Cradock, J. Brockenbrough, G. Liu, G. Monroy, R. Nolan, N. D. Shemonski, J. Putney, D. Darga, A. Cittadine, P. S. Carney, and S. A. Boppart, "Intraoperative hand-held probe-based imaging of in situ breast tumor margins and lymph nodes using OCT and ISAM," presented at the SPIE Photonics West BIOS, San Francisco, CA, 2013.

[20] A. M. Zysk, E. J. Chaney, and S. A. Boppart, "Refractive index of carcinogen-induced rat mammary tumours," *Physical in Medicine and Biology*, vol. 51, pp. 2165-77, May 2006.

[21] P. P. Provenzano, K. W. Eliceiri, J. M. Campbell, D. R. Inman, J. G. White, and P. J. Keely, "Collagen reorganization at the tumor-stromal interface facilitates local invasion," *BMC Medicine*, vol. 4, Dec 2006.

[22] M. W. Conklin, J. C. Eickhoff, K. M. Riching, C. A. Pehlke, K. W. Eliceiri, P. P. Provenzano, A. Friedl, and P. J. Keely, "Aligned collagen is a prognostic signature for survival in human breast carcinoma," *American Journal of Pathology*, vol. 178, pp. 1221-1232, Mar 2011.

[23] M. Born and E. Wolf, *Principles of Optics: Electromagnetic Theory of Propagation, Interference and Diffraction of Light*, 7th ed. Cambridge, UK: Cambridge University Press, 1999.

[24] J. F. deBoer, T. E. Milner, M. J. C. van Gemert, and J. S. Nelson, "Two-dimensional birefringence imaging in biological tissue by polarization-sensitive optical coherence tomography," *Optics Letters*, vol. 22, pp. 934-936, Jun 1997.

[25] S. K. Nadkarni, M. C. Pierce, B. H. Park, J. F. de Boer, P. Whittaker, B. E. Bouma, J. E. Bressner, E. Halpern, S. L. Houser, and G. J. Tearney, "Measurement of collagen and smooth muscle cell content in atherosclerotic plaques using polarization-sensitive optical coherence tomography," *Journal of the American College of Cardiology*, vol. 49, pp. 1474-1481, Apr 2007.

[26] Y. Verma, M. Gautam, K. D. Rao, M. K. Swami, and P. K. Gupta, "Imaging of human breast tissue using polarization sensitive optical coherence tomography," *Laser Physics*, vol. 21, pp. 2143-2148, Dec 2011.

[27] P. H. Tomlins and R. K. Wang, "Theory, developments and applications of optical coherence tomography," *Journal of Physics D: Applied Physics*, vol. 38, p. 2519, 2005.

[28] R. Huber, M. Wojtkowski, and J. G. Fujimoto, "Fourier domain mode locking (FDML): A new laser operating regime and applications for optical coherence tomography," *Optics Express*, vol. 14, pp. 3225-3237, Apr 2006.

[29] J. F. de Boer, B. Cense, B. H. Park, M. C. Pierce, G. J. Tearney, and B. E. Bouma, "Improved signal-to-noise ratio in spectral-domain compared with time-domain optical coherence tomography," *Optics Letters*, vol. 28, pp. 2067-2069, Nov 2003.

[30] M. A. Choma, M. V. Sarunic, C. H. Yang, and J. A. Izatt, "Sensitivity advantage of swept source and Fourier domain optical coherence tomography," *Optics Express*, vol. 11, pp. 2183-2189, Sep 2003.

[31] W. Drexler and J. G. Fujimoto, *Optical Coherence Tomography: Technology and Applications*. New York: Springer, 2008.

[32] J. M. Schmitt, A. Knuttel, M. Yadlowsky, and M. A. Eckhaus, "Optical-coherence tomography of a dense tissue: Statistics of attenuation and backscattering," *Physics in Medicine and Biology*, vol. 39, pp. 1705-1720, Oct 1994.

[33] R. C. Haskell, F. D. Carlson, and P. S. Blank, "Form birefringence of muscle," *Biophysical Journal*, vol. 56, pp. 401-413, Aug 1989.

[34] J. J. Pasquesi, S. C. Schlachter, M. D. Boppart, E. Chaney, S. J. Kaufman, and S. A. Boppart, "In vivo detection of exercise-induced ultrastructural changes in genetically-altered murine skeletal muscle using polarization-sensitive optical coherence tomography," *Optics Express*, vol. 14, pp. 1547-1556, Feb 2006.

[35] E. Hecht, *Optics*, 4th ed. San Francisco, CA: Addison-Wesley, 2002.

[36] H. H. Hurwitz and R. C. Jones, "A new calculus for the treatment of optical systems II. Proof of three general equivalence theorems," *Journal of the Optical Society of America,* vol. 31, pp. 493-499, Jul 1941.

[37] R. C. Jones, "A new calculus for the treatment of optical systems I. Description and discussion of the calculus," *Journal of the Optical Society of America,* vol. 31, pp. 488-493, Jul 1941.

[38] R. C. Jones, "A new calculus for the treatment of optical systems IV," *Journal of the Optical Society of America,* vol. 32, pp. 486-493, Aug 1942.

[39] R. C. Jones, "A new calculus for the treatment of optical systems VII. Properties of the N-matrices," *Journal of the Optical Society of America,* vol. 38, pp. 671-685, Aug 1948.

[40] B. Mellish. (2006). *Waveplate* [Online]. Available: http://en.wikipedia.org/wiki/File:Waveplate.png

[41] S. L. Jiao, W. R. Yu, G. Stoica, and L. H. V. Wang, "Optical-fiber-based Mueller optical coherence tomography," *Optics Letters,* vol. 28, pp. 1206-1208, Jul 2003.

[42] G. G. Stokes, "On the change of refrangibility of light," *Philosophical Transactions of the Royal Society of London,* vol. 142, pp. 463-562, 1852.

[43] R. C. Jones, "A new calculus for the treatment of optical systems V. A more general formulation, and description of another calculus," *Journal of the Optical Society of America,* vol. 37, pp. 107-110, Feb 1947.

[44] J. F. de Boer and T. E. Milner, "Review of polarization sensitive optical coherence tomography and Stokes vector determination," *Journal of Biomedical Optics,* vol. 7, pp. 359-371, Jul 2002.

[45] S. G. Adie, T. R. Hillman, and D. D. Sampson, "Detection of multiple scattering in optical coherence tomography using the spatial distribution of Stokes vectors," *Optics Express,* vol. 15, pp. 18033-18049, Dec 2007.

[46] B. J. Davis, S. C. Schlachter, D. L. Marks, T. S. Ralston, S. A. Boppart, and P. S. Carney, "Nonparaxial vector-field modeling of optical coherence tomography and interferometric synthetic aperture microscopy," *Journal of the Optical Society of America A,* vol. 24, pp. 2527-2542, Sep 2007.

[47] B. H. Park, M. C. Pierce, B. Cense, and J. F. de Boer, "Optic axis determination accuracy for fiber-based polarization-sensitive optical coherence tomography," *Optics Letters,* vol. 30, pp. 2587-2589, Oct 2005.

[48] M. R. Hee, D. Huang, E. A. Swanson, and J. G. Fujimoto, "Polarization-sensitive low-coherence reflectometer for birefringence characterization and ranging," *Journal of the Optical Society of America B,* vol. 9, pp. 903-908, Jun 1992.

[49] E. Gotzinger, M. Pircher, and C. K. Hitzenberger, "High speed spectral domain polarization sensitive optical coherence tomography of the human retina," *Optics Express,* vol. 13, pp. 10217-10229, Dec 2005.

[50] B. Baumann, W. Choi, B. Potsaid, D. Huang, J. S. Duker, and J. G. Fujimoto, "Swept source / Fourier domain polarization sensitive optical coherence tomography with a passive polarization delay unit," *Optics Express,* vol. 20, pp. 10229-10241, Apr 2012.

[51] C. Hitzenberger, E. Goetzinger, M. Sticker, M. Pircher, and A. Fercher, "Measurement and imaging of birefringence and optic axis orientation by phase resolved polarization sensitive optical coherence tomography," *Optics Express,* vol. 9, pp. 780-90, Dec 2001.

[52] G. D. VanWiggeren and R. Roy, "Transmission of linearly polarized light through a single-mode fiber with random fluctuations of birefringence," *Applied Optics,* vol. 38, pp. 3888-3892, Jun 1999.

[53] C. E. Saxer, J. F. de Boer, B. H. Park, Y. H. Zhao, Z. P. Chen, and J. S. Nelson, "High-speed fiber-based polarization-sensitive optical coherence tomography of in vivo human skin," *Optics Letters,* vol. 25, pp. 1355-1357, Sep 2000.

[54] M. K. Al-Qaisi and T. Akkin, "Polarization-sensitive optical coherence tomography based on polarization-maintaining fibers and frequency multiplexing," *Optics Express,* vol. 16, pp. 13032-13041, Aug 2008.

[55] E. Götzinger, B. Baumann, M. Pircher, and C. K. Hitzenberger, "Polarization maintaining fiber based ultra-high resolution spectral domain polarization sensitive optical coherence tomography," *Optics Express,* vol. 17, pp. 22704-22717, Dec 2009.

[56] J. Zhang, S. G. Guo, W. G. Jung, J. S. Nelson, and Z. P. Chen, "Determination of birefringence and absolute optic axis orientation using polarization-sensitive optical coherence tomography with PM fibers," *Optics Express,* vol. 11, pp. 3262-3270, Dec 2003.

[57] J. E. Roth, J. A. Kozak, S. Yazdanfar, A. M. Rollins, and J. A. Izatt, "Simplified method for polarization-sensitive optical coherence tomography," *Optics Letters,* vol. 26, pp. 1069-1071, Jul 2001.

[58] S. L. Jiao and L. H. V. Wang, "Jones-matrix imaging of biological tissues with quadruple-channel optical coherence tomography," *Journal of Biomedical Optics,* vol. 7, pp. 350-358, Jul 2002.

[59] B. H. Park, M. C. Pierce, B. Cense, and J. F. de Boer, "Jones matrix analysis for a polarization-sensitive optical coherencetomography system using fiber-optic components," *Optics Letters,* vol. 29, pp. 2512-2514, Nov 2004.

[60] S. Makita, M. Yamanari, and Y. Yasuno, "Generalized Jones matrix optical coherence tomography: Performance and local birefringence imaging," *Optics Express,* vol. 18, pp. 854-876, Jan 2010.

[61] Z. H. Lu and S. J. Matcher, "Absolute fast axis determination using non-polarization-maintaining fiber-based polarization-sensitive optical coherence tomography," *Optics Letters,* vol. 37, pp. 1931-1933, Jun 2012.

[62] C. Fan and G. Yao, "Single camera spectral domain polarization-sensitive optical coherence tomography using offset B-scan modulation," *Optics Express,* vol. 18, pp. 7281-7287, Mar 2010.

[63] Thorlabs. (2011). *PSOCT-1300* [Online]. Available: http://www.thorlabs.com/thorcat/18100/PSOCT-1300-Manual.pdf

[64] L. Chin, X. Yang, R. A. McLaughlin, P. B. Noble, and D. D. Sampson, "En face parametric imaging of tissue birefringence using polarization-sensitive optical coherence tomography," *Journal of Biomedical Optics,* vol. 18, pp. 066005-1-066005-6, Jun 2013.

[65] R. Huber, D. C. Adler, and J. G. Fujimoto, "Buffered Fourier domain mode locking: Unidirectional swept laser sources for optical coherence tomography imaging at 370,000 lines/s," *Optics Letters,* vol. 31, pp. 2975-2977, Oct 2006.

[66] D. C. Adler, S.-W. Huang, R. Huber, and J. G. Fujimoto, "Photothermal detection of gold nanoparticlesusing phase-sensitive optical coherencetomography," *Optics Express,* vol. 16, pp. 4376-4393, Mar 2008.

[67] T. Meng-Tsan, L. Ya-Ju, Y. Yung-Chi, K. Che-Yen, C. Feng-Yu, and J. D. Lee, "Quantitative phase imaging with swept-source optical coherence tomography for optical measurement of nanostructures," *IEEE Photonics Technology Letters,* vol. 24, pp. 640-642, April 2012.

[68] H. C. Hendargo, R. P. McNabb, A.-H. Dhalla, N. Shepherd, and J. A. Izatt, "Doppler velocity detection limitations in spectrometer-based versus swept-source optical coherence tomography," *Biomedical Optics Express,* vol. 2, pp. 2175-2188, Aug 2011.

[69] A. W. Schaefer, J. J. Reynolds, D. L. Marks, and S. A. Boppart, "Real-time digital signal processing-based optical coherence tomography and Doppler optical coherence tomography," *IEEE Trans. on Biomedical Engineering,* vol. 51, pp. 186-190, Jan 2004.

[70] K. Zhang and J. U. Kang, "Real-time 4D signal processing and visualization using graphics processing unit on a regular nonlinear-k Fourier-domain OCT system," *Optics Express,* vol. 18, pp. 11772-11784, May 2010.

[71] J. A. Izatt, M. D. Kulkami, S. Yazdanfar, J. K. Barton, and A. J. Welch, "In vivo bidirectional color Doppler flow imaging of picoliter blood volumes using optical coherence tomograghy," *Optics Letters,* vol. 22, pp. 1439-1441, Sep 1997.

[72] T. S. Ralston, D. L. Marks, P. S. Carney, and S. A. Boppart, "Interferometric synthetic aperture microscopy," *Nature Physics,* vol. 3, pp. 129-134, Feb 2007.

[73] A. Ahmad, M. Ali, F. South, G. L. Monroy, S. G. Adie, N. Shemonski, P. S. Carney, and S. A. Boppart, "Interferometric synthetic aperture microscopy implementation on a floating point multi-core digital signal processer," in *Proc. SPIE 8571, Optical Coherence Tomography and Coherence Domain Optical Methods in Biomedicine XVII*, San Francisco, CA, 2013, pp. 857134-1-857134-9.

[74] Y. Jian, K. Wong, and M. V. Sarunic, "Graphics processing unit accelerated optical coherence tomography processing at megahertz axial scan rate and high resolution video rate volumetric rendering," *Journal of Biomedical Optics,* vol. 18, pp. 026002-1-026002-4, Feb 2013.

[75] A. Ahmad, N. D. Shemonski, S. G. Adie, H. S. Kim, W. M. W. Hwu, P. S. Carney, and S. A. Boppart, "Real-time in vivo computed optical interferometric tomography," *Nature Photonics,* vol. 7, pp. 445-449, Jun 2013.

[76] M. Sylwestrzak, D. Szlag, M. Szkulmowski, I. Gorczynska, D. Bukowska, M. Wojtkowski, and P. Targowski, "Four-dimensional structural and Doppler optical coherence tomography imaging on graphics processing units," *Journal of Biomedical Optics,* vol. 17, Oct 2012.

[77] AlazarTech. (2013). *ATS9350* [Online]. Available: http://www.alazartech.com/products/ATS9350_v_1_6a.pdf

[78] NVIDIA. (2011). *CUDA Toolkt 4.1* [Online]. Available: https://developer.nvidia.com/cuda-toolkit-41-archive

[79] G. J. Liu, J. Zhang, L. F. Yu, T. Q. Xie, and Z. P. Chen, "Real-time polarization-sensitive optical coherence tomography data processing with parallel computing," *Applied Optics,* vol. 48, pp. 6365-6370, Nov 2009.

[80] L. C. U. Junqueira, G. Bignolas, and R. R. Brentani, "Picrosirius staining plus polarization microscopy, a specific method for collagen detection in tissue-sections," *Histochemical Journal,* vol. 11, pp. 447-455, 1979.

[81] D. Dayan, Y. Hiss, A. Hirshberg, J. J. Bubis, and M. Wolman, "Are the polarization colors of picrosirius red-stained collagen determined only by the diameter of the fibers?," *Histochemistry,* vol. 93, pp. 27-9, 1989.

[82] B. Young and J. W. Heath, *Wheater's Functional Histology*, 4th ed. New York: Churchill Livingstone, 2000.

[83] N. C. Institute. (2013). *Ductal carcinoma in situ* [Online]. Available: http://www.cancer.gov/cancertopics/pdq/treatment/breast/healthprofessional/page4